Investigation of the fast flux test facility transient behavior during a loss of flow without scram test

Cristiano Ciurluini, Michele Marra, Vincenzo Narcisi, Gianfranco Caruso, Fabio Giannetti[*]

DIAEE – Nuclear Engineering Research Group, Sapienza University of Rome, Corso Vittorio Emanuele II, 244, 00186 Rome, Italy

ARTICLE INFO

ABSTRACT

A Coordinated Research Project (CRP) on the benchmark analysis of Fast Flux Test Facility (FFTF) Loss of Flow Without Scram (LOFWOS) has been held under the sponsorship of the International Atomic Energy Agency. The CRP aims to improve understanding of loss of flow events in fast reactors, as well as to assess capabilities of existing computer codes against experimental data. FFTF is a 400 MWth Sodium-cooled Fast Reactor (SFR) owned by the U.S. Department of Energy, operated from 1980 to 1992. The CRP involves the LOFWOS Test #13, belonging to a series of unprotected transients performed as part of the Passive Safety Testing program. In this framework, the Nuclear Engineering Research Group of Sapienza University of Rome has developed an integrated multiphysics modelling based on a coupled approach with RELAP5-3D© (thermal-hydraulics) and PHISICS (neutron-kinetics) codes. The present paper discusses the results obtained by the authors after the participation in the benchmark open phase. As suggested by the organizers, a two-step methodology was followed. Firstly, calculations were run by imposing the reactor power as boundary condition and focusing on the FFTF thermal–hydraulic behaviour. A good accordance was detected between the numerical results and the experimental data, above all for what concerns the reference core outlet temperatures. Then, the simulations were repeated by using a coupled approach. Calculation outcomes demonstrated the capability of the selected code suite (PHISICS/RELAP5-3D®) to reproduce the reactor transient behavior and its suitability to be used as an effective numerical tool to simulate liquid metal fast reactors accidental scenarios where thermal–hydraulic and neutron-kinetic phenomena are strongly coupled.

1. Introduction

The Generation IV (GEN IV) International Forum was founded in 2009 as a worldwide co-operation framework for the development of the fourth generation of nuclear reactors. Technology goals have been defined for GEN IV nuclear systems in four broad areas: sustainability, safety and reliability, economics, proliferation resistance and physical protection (OECD Nuclear Energy Agency, 2014). The fast breeder reactors were selected as one of the most promising options since they

allow a closed fuel cycle, the management of radioactive waste (by reducing the proportion of long-lived isotopes contained in them) and the consume of weapons-grade plutonium (burning it as nuclear fuel).

For the purpose of the fast reactors analysis, the presence of an intense neutron flux within the core leads to the need of Neutron-Kinetic (NK) and Thermal-Hydraulic (TH) coupled simulations to study operating and accidental conditions which may interest the nuclear power plant. The capability to perform these calculations is one of the main open topics in the GEN IV fast reactors development. From the point of

view of the reactor safety, one of the major issues is the possibility to study complex accidental sequences, such as considering a postulated "traditional" accident in the case of failure of the quick shut-down system. This category of potential severe accident scenarios is named "unprotected accidents". From the neutronic point of view, the most common approach adopted so far to study these transient scenarios is based on a diffusion approximation coupled with 1-D or 2-D thermal hydraulics. The comparison with experimental data obtained during tests in EBR II and Phénix reactors were used in the past years to validate this approach, (Del Nevo and Martelli, 2016; Tenchine et al., 2013). Unfortunately, 1D codes do not allow to predict some local aspects of the core behaviour and, for this, a more detailed 3D study is needed. For this reason, in 2018, the International Atomic Energy Agency (IAEA) started a Coordinated Research Project (CRP) aimed at the validation of NK/TH coupled approaches by comparing numerical results with the experimental data coming from the Fast Flux Test Facility (FFTF) (IAEA, 2018). The Loss Of Flow WithOut Scram (LOFWOS) Test #13, performed at the facility in 1986, was selected.

Many international institutions participated in the benchmark exercise, proposing several coupled approaches (Morelová et al., 2023). Some participants took the opportunity to validate their in-house codes, such as SAC-3D (North China Electric Power University, Lyu et al., 2021), SAS4/SASSYS-1 (Argonne National Laboratory, that is also the benchmark organizer, Rivas et al., 2021), SAM (Argonne National Laboratory, Liu et al.,2023), GAMMA+ (Korea Atomic Energy Research Institute, Hong et al., 2024), Super-COPD (Japan Atomic Energy Agency, Hamase et al., 2024), SIMMER (Karlsruhe Institute of Technology, Chen and Rineiski, 2023), the code suite PERT3D/FARCOB (NK) – DYANA-P (TH) (Indira Gandhi Centre for Atomic Research, Vikram et al., 2023). Other institutions preferred to develop a coupled methodology based on state-of-the-art computational tools. Helmholtz-Zentrum Dreden-Rossendof relied on the continuous-energy Monte Carlo code Serpent, the three-dimensional nodal diffusion code DYN3D, and the thermal hydraulics system code ATHLET (Nikitin et al., 2024). Xi'an Jiaotong University, in collaboration with the Nuclear Power Institute of China, combined the Monte Carlo code OpenMC and the in-house system thermal hydraulic code THACS (Zhou et al., 2023). École Polytechnique Fédérale de Lausanne and its partner, the Wuhan Second Ship Design and Research Institute, prepared a point-kinetics model in OpenFOAM and, as a proof of concept, integrated it in the GeN-Foam Multiphysics code (Radman et al., 2022). The Paul Scherrer Institute developed a point kinetics model in TRACE, whose reactivity feedback parameters were computed with Serpent-2 Monte Carlo code (Wang et al., 2021).

Also, the Nuclear Engineering Research Group (NERG) of Sapienza University of Rome followed this second approach. The selected code suite consists of: the U.S. Nuclear Regulatory Commission best-estimate thermal–hydraulic system code RELAP5-3D© (The RELAP5-3D© Code Development Team, 2015a), and the PHISICS reactor analysis toolkit, developed since 2011 at the Idaho National Laboratory to perform advanced neutron transport calculations (Alfonsi et al., 2019). The PHISICS/RELAP5-3D® coupled codes have been already used to simulate transients of VVER-440 Russian pressurized water reactors (Balestra et al., 2016) and High Temperature Gas-cooled Reactors (Balestra et al., 2017). In addition, they have been employed for the preliminary NK/TH calculations of unprotected transients in the Advanced Lead-cooled Fast Reactor European Demonstrator (Ciurluini et al., 2020).

In the current work, the application of the NERG coupled methodology to the IAEA CRP involving the FFTF transient analysis is discussed. The paper is articulated as following. Section 2 deals with the description of the facility and the related experimental campaign, with a particular focus on LOFWOS Test #13. The RELAP5-3D© TH model and the PHISICS NK nodalization are presented in sections 3.1 and 3.3, respectively. The main results obtained by NERG at the end of the benchmark open phase are discussed in sections 3.2 and 3.4. As suggested by the organizers, a two-step methodology was followed. Firstly,

simulations were run by imposing the reactor power as boundary condition and focusing on the FFTF thermal–hydraulic behaviour. Then, the calculations were repeated by using a coupled approach. The main conclusions related to the current simulation activity are drawn in section 4.

2. Description of the facility and the experimental campaign

2.1. Facility overview

FFTF was a sodium-cooled fast reactor designed by Westinghouse Electric Corporation and owned by the U.S Department of Energy (Wootan et al., 2017a). It was installed at Handford site in Washington and operated from 1980, when the first criticality was reached, up to 1992. It was shut down in 1993. It was a loop-type SFR with a rated thermal power of 400 MW. The reactor overview is shown by Fig. 1a. Low-pressure liquid sodium was the primary coolant. The Heat Transport System (HTS) was constituted by three parallel loops, each one provided with an Intermediate Heat Exchanger (IHX). These components were foreseen to physically separate the activated liquid metal flowing through the core from the nonradioactive secondary sodium. Since FFTF was not supposed to produce electricity, thermal power was finally discharged to the ultimate heat sink, represented by twelve sodium-air Dump Heat Exchangers (DHX, four per loop).

The reactor core, whose overview is provided in Fig. 2, consisted of 199 hexagonal assemblies (Sumner, 2018). During the experimental campaign considered for this benchmark exercise, they were divided in different types, in particular: Driver Fuel Assemblies (DFA), In Core Shim Assembly (ICSA), reflector assemblies (REFL), Control Rods/Safety Rods (CR/SR), Material Open Test Assembly (MOTA), Fracture Mechanics Assembly (FMA) and Gas Expansion Modules (GEM). Core assemblies were distributed in nine rows, including the central assembly counted as the first one. The seven inner rows were allocated in the core basket, while the lasting two were supported by the inner radial shield support, located at a slightly higher elevation. This means that the outermost reflector assemblies are slightly shorter with respect to the others. The active core was composed of 80 DFAs, all placed in the first six rows. Each assembly was made up of 217 mixed oxide fuel pins, with an active length of 914 mm (red region in Fig. 1a). Fast response thermocouple (TC) packages were installed within a duct placed above some selected DFAs, called Proximity Instrumented Open Test Assemblies (PIOTA), (Sumner, 2018). This acquisition of core outlet temperature was essential in case of fast transients, as the one object of this benchmark exercise. In LOFWOS Test #13, two PIOTAs were present in the core, located in rows two and six, respectively. They are circled in red in Fig. 2. ICSA and MOTA occupied two seats in row four. The former was identical to a DFA but with stainless steel pins substituting the fuel pins. Instead, MOTA was an instrumented open test assembly. Core reactivity was kept under control by using three SRs (row three) and six CRs (row five). Active core was radially surrounded by reflector assemblies, from row seven to row nine. A FMA was situated in row seven to continue irradiation of FFTF archives and surveillance program specimens (Wootan et al., 2017b). Still in row seven, nine seats were reserved to GEMs. These assemblies consisted in a 3.658 m long pipe, sealed at the top, open at the bottom and filled with sodium and cover gas (argon). During normal operations, the sodium free level within the component was fixed by the sodium head and the primary pump discharge pressure. The GEM gas volume was compressed above the Top of Active Fuel (TAF). In case of loss of primary flow, pressure at core inlet decreased since pump head contribute was missing. This caused the gas expansion within GEM assemblies. The correspondent sodium level dropped below the Bottom of Active Fuel (BAF), determining passive negative reactivity feedback. In fact, being GEMs located in row seven (just beyond DFAs in radially outward direction), a decrease of their sodium level led to higher radial neutron leakage, corresponding to a negative reactivity insertion (Nguyen, 1990). Finally, the region between the outer row and
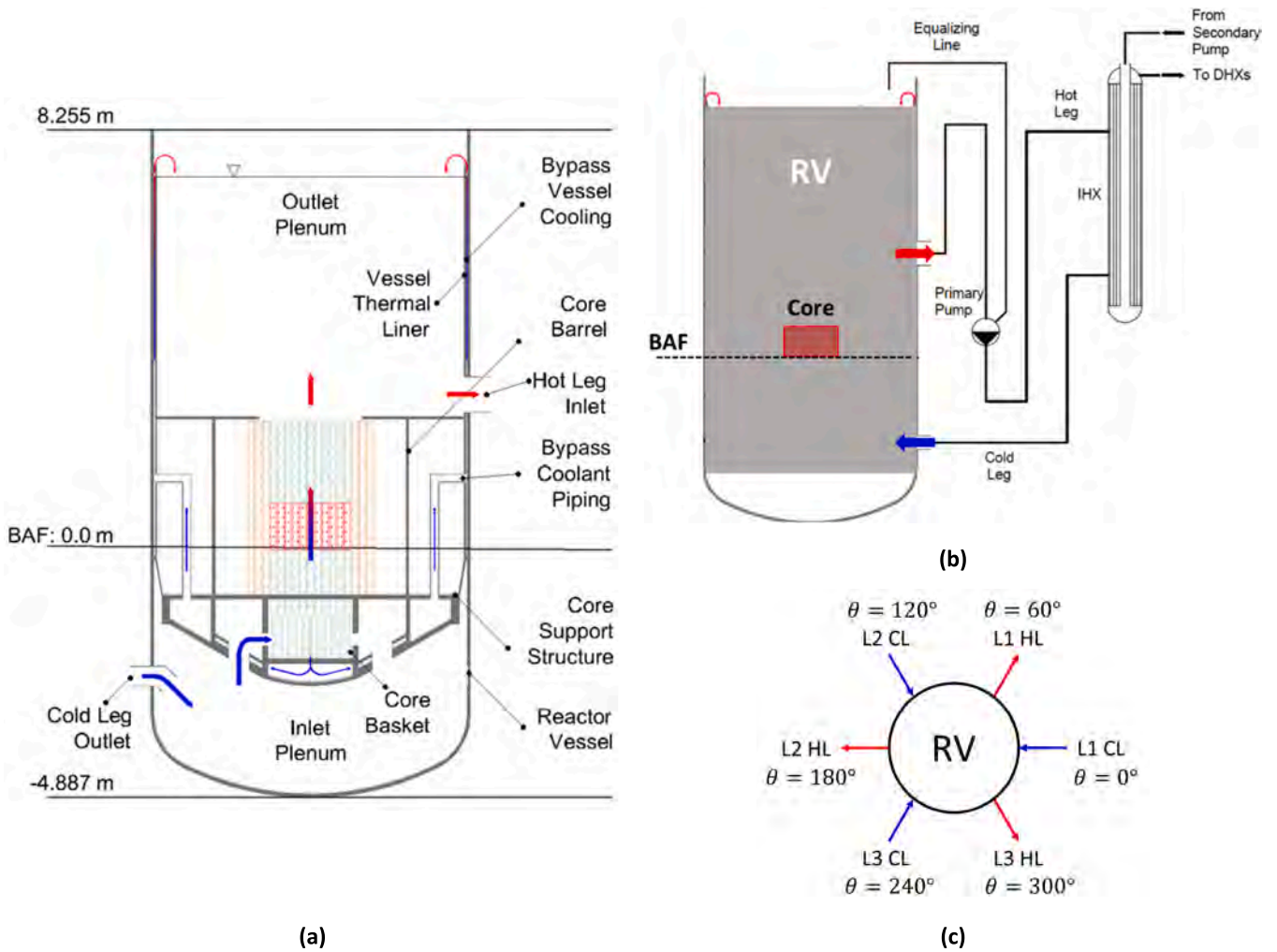
Fig. 1. Overview of FFTF RV (a) and its connections with the HTS primary loops (b and c). In figure (b), only one of the three loops is represented. In figure (c), L1, L2 and L3 are the three HTS primary loops, HL stands for Hot Leg and CL for Cold Leg.
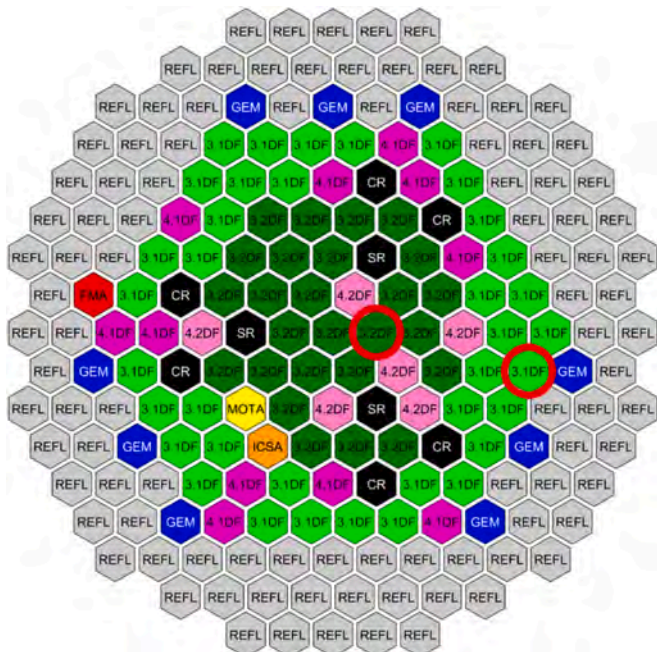

Fig. 2. Overview of FFTF core. Row 2 and row 6 PIOTAs are circled in red.

the core barrel was filled with shield plates and the core restraint system. The latter permitted core radial expansion during power transients, resulting in overall negative reactivity feedback.

Reactor Vessel (RV) had a cylindrical shape with a bottom torospherical head (see Fig. 1a). Three deflector elbows located at the vessel bottom connected the component to the primary loop cold legs, allowing the sodium to enter the RV. The three entrances were equally distributed along the azimuthal coordinate at a relative angular distance of 120°. The elbows layout guided cold fluid to the bottom of the reactor, enhancing mixing. From the inlet plenum, primary coolant was driven to the Core Support Structure (CSS). It enters a mid-lateral annular volume through twelve holes (only two are visible in Fig. 1a). The core basket was hosted within the CSS central volume and conceived to allocate most of the assembly receptacles (as discussed above). Once reached the CSS, multiple flow paths were available for the primary flow. In particular, the main stream passed from the CSS to the core basket thanks to dedicated windows in the lateral walls of the component. Minor flows were directed to the external reflector assemblies (row eight and nine) and the channels between radial shield blocks. Flow arrived in the core basket was at its time subdivided in two contributes. The majority was addressed to the core assemblies while a small fraction was supposed to cool the reactor vessel and the vessel thermal liner. Inlet holes associated to core assemblies were located nearly at the top of core basket. Instead, vessel cooling flow rate was diverted to the bottom of the component and drawn in the peripheral region of the core support structure through twelve sloped holes. From there, three bypass coolant

pipes led sodium to the annular region between the reactor vessel and the vessel thermal liner. All the primary flow contributes were finally collected in the outlet plenum and exited the RV through three primary outlet pipes, symmetrically disposed along the vessel circumference. With respect to the RV inlets, the corresponding outlets are translated of 60° along the azimuthal direction (see Fig. 1c). A clear indication of the multiple flow paths followed by the overall primary flow within the RV is provided by arrows reported in Fig. 1a. An argon atmosphere was ensured above the outlet plenum to avoid the occurrence of dangerous air-sodium reactions. In Fig. 1a the outlet plenum is represented as a large empty volume. Although, several devices were here situated, such as control rod drivelines, in-vessel handling machine, instrument tree and low-level flux monitoring system. Nevertheless, details on these components were not provided in the benchmark specifications (Sumner, 2018). For this, they have not been included in the schematic view of the reactor.

The FFTF RV was provided with three primary cooling loops. Their layout was almost identical, and it is shown in Fig. 1b and Fig. 3 (Sumner, 2018). Hot legs ran from the reactor vessel outer wall to the IHXs inlet. Each one was equipped with a vertical, free surface centrifugal pump. Cold legs returned primary sodium to the RV inlet plenum. Equalizing lines (one per loop, see Fig. 1b) were also foreseen to connect the RV argon cover gas to primary pumps. In this way, the argon pressure at the top of reactor vessel, as well as within the circulators was equalized. During normal operations, different sodium levels characterize the outlet plenum and the equalizing lines due to the pressure drops in the loop section going from the RV to the primary pumps. The IHXs were vertical, counterflow, shell and tube heat exchangers. Primary sodium entered laterally and flowed downwards through the shell side, while it was cooled. Primary cold leg was connected at the component bottom. Instead, secondary cold leg was located at the IHX top. Cold fluid moved through a central downcomer, reaching the bottom head. Then, it was distributed in the tube bundle (1540 tubes per IHX), where rose to the upper head while it was heated up. Here, the hot secondary sodium exited the IHX and flowed through the hot leg directed to the DHXs. The active height was of 4.2 m. Secondary pumps

(one per loop) were located on the cold legs.

2.2. Experimental campaign and qualitative description of LOFWOS Test #13

In July 1986, an extensive experimental campaign, named Passive Safety Testing Program, was conducted in FFTF. It was aimed at evaluating the SFR performances under an unprotected loss of flow condition (Sumner, 2018). For this, thirteen loss of flow without scram tests were performed with the goal of assessing the liquid metal reactor safety margins, providing data for computer code validation, and demonstrating the passive safety benefits of specific design features, such as the GEMs. Among them, the LOFWOS Test #13 was selected for benchmarking purposes (Sumner, 2018). Before the Start of the Transient (SoT), reactor power was slightly below the 50 % of the nominal value, while primary pump provided the 100 % of the rated mass flow. These conditions were kept for about seven and a half hours to allow the establishment of steady state. The core inlet temperature was maintained 44 °C below the nominal value to avoid excessive peak fuel temperature during the LOFWOS transient and respect the safety limits. The reactor initial conditions before the start of the LOFWOS Test #13 are summarized in Table 1 (Sumner, 2018).

The overall transient evolution can be split in five different

Table 1
Initial conditions for LOFWOS Test #13 (Sumner, 2018).

Parameter	Units	Value
Total power	MW$_{th}$	199.2
Core inlet temperature	°C	317.2
Total primary Mass Flow Rate	kg/s	2202.24
RV Sodium level[1]	m	7.341
GEM sodium level[1]	m	1.213
Average DHX outlet temperature[2]	°C	301.5
Total secondary Mass Flow Rate	kg/s	2202.2

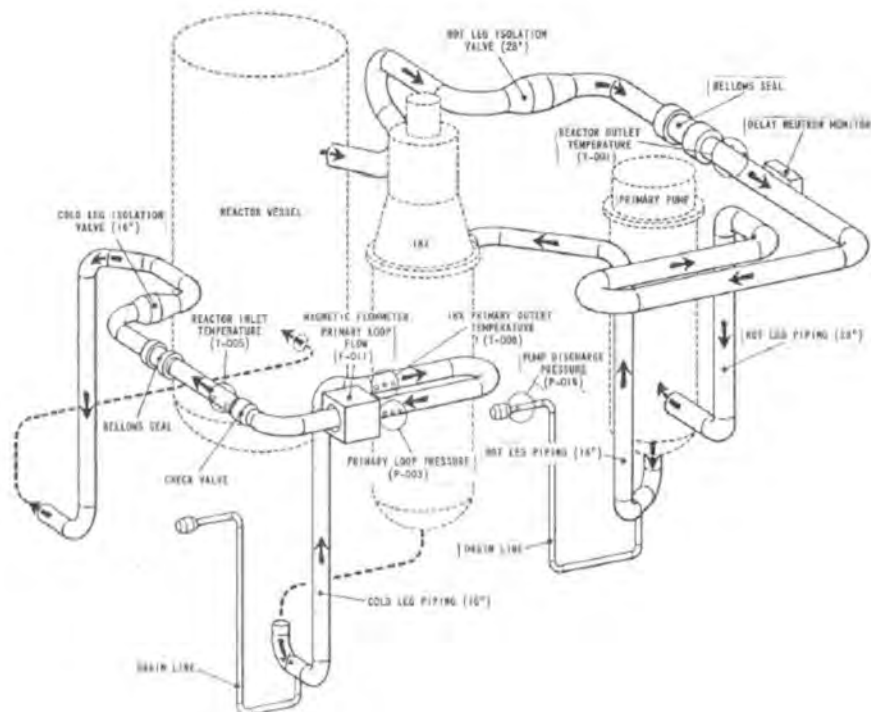[1] Elevation relative to the BAF.
[2] Before fan speed decrease.

Fig. 3. Overview of FFTF HTS primary loop, one of three (Sumner, 2018).

Phenomenological Windows (PhW). The first one lasts two minutes and occurs before the primary pump trip, considered as the official SoT (t = 0 s). Approximately one minute before the SoT, DHXs fan speed was reduced. Instead, the secondary pumps speed was kept constant for the whole experiment. These operations produced an increase of the secondary cold leg temperatures but were carried out to maintain a relatively constant core inlet temperature for the overall transient (Sumner, 2018).

The test started with the simultaneous trip of the three primary pumps. The plant protection system was bypassed to avoid the reactor scram. The primary flow coastdown was ruled by the kinetic energy stored in the form of pump inertia. The time trend throughout the experiment of the primary pumps speed was provided as boundary condition to the benchmark participants (Sumner, 2018). In the first seconds after the SoT (PhW2), the rapid drop of the primary flow led the power-to-flow ratio to rise, producing a first peak in the core outlet temperature. The core structural temperature excursion caused a negative reactivity feedback due to the Doppler effect. Moreover, the primary flow decrease reduced the pressure at the core inlet. Consequently, the GEM level lowered from above the TAF to below the BAF, provoking an additional negative reactivity feedback due to the higher radial neutron leakages. Finally, the thermal expansion of the control and safety rods (due to the core heating) provokes a correspondent component insertion within the active length providing another important negative contribute to the overall reactivity (PhW3). These negative feedbacks drove the reactor power shutdown. During the power coastdown, there was an initial phase (PhW4) where the power was prevalent on the mass flow and the corresponding ratio increased. This produced the second (and maximum) temperature peak at the core outlet. Then, in the final part of the transient (PhW5), where only decay heat was still present and the natural circulation was completely established in the primary loops, the power-to-flow ratio value reverted, and the long-term cooling of the reactor took place. The timing associated with the five phenomenological windows are collected in Table 2, together with the main events occurring in each PhW.

Referring to the plant instrumentation, special fast response TCs were associated with the two PIOTAs present in the core. Their response time was of 3 s. Instead, their measurement uncertainty was not provided by the benchmark specifications. Outside the RV, Resistance Temperature Detectors (RTD) were used to monitor the sodium temperatures in all the primary and secondary loops hot and cold legs. They were characterized by a response time of 5 s and an accuracy of $\pm 1.6\,°C$. The sodium mass flow rate was measured in each primary and secondary loop thanks to permanent magnet flow meters, installed in the cold leg piping. Their response time and measurement uncertainty were not given. Exact sensor locations were provided by the benchmark specifications (Sumner, 2018). For primary loops, they are visible in Fig. 3.

Table 2
Definition of the main Phenomenological Windows for LOFWOS Test #13.

PhW	Time interval (s)	Description
1	−120 – 0	Decrease of DHXs fan speed and increase of the secondary cold leg temperatures.
2	0–9	Increase of the Power-to-flow ratio and occurrence of the first core outlet temperature peak.
3	9–25	Power coastdown ruled by negative reactivity feedbacks (i.e., Doppler effect and GEM sodium level drop from TAF to BAF).
4	25–100	GEM level below BAF. New increase of the Power-to-flow ratio and occurrence of the second (and maximum) core outlet temperature peak.
5	100–End of transient (900 s)	Long-term cooling due to natural circulation

3. IAEA CRP open phase simulation results

3.1. TH model

3.1.1. Core model

The thermal–hydraulic model for the FFTF reactor was developed and refined by NERG throughout the overall benchmark duration. In Narcisi et al. (2021) a preliminary version of the RELAP5-3D® input deck is described. It was used to run stand-alone TH simulations and perform sensitivity studies aimed at a deeper understanding of some of the main TH phenomena occurring during LOFWOS Test #13, i.e., outlet plenum thermal stratification, simulation of the sodium-argon interfaces, etc. The lessons learned from this activity were used to furtherly upgrade the RELAP5-3D® input deck, whose ultimate version is discussed below. The final open phase results were obtained with this nodalization. In the following, some aspects of the TH model are only briefly recalled since unchanged with respect to the description done in Narcisi et al. (2021). The discussion is mainly focused on the new features implemented.

The FFTF core is modelled following the assembly-by-assembly approach, thus associating an equivalent pipe to each Sub-Assembly (SA). It simulates the overall sodium flow path within the component, differentiated for each assembly type (DFA, REFL, CR/SR, GEM, ICSA, MOTA, FMA). Sliced approach is considered for the overall core. This methodology foresees the usage of the same mesh height (or submultiple) for the vertical control volumes belonging to the different nodalization regions located at the same axial level. (Mascari et al., 2011). The vertical nodes constituting the axial nodalization were chosen to be consistent with the assembly design described in the benchmark specifications (Sumner, 2018). The adoption of the sliced approach improves the code capability to reproduce the natural circulation, whose correct simulation is of primary importance for LOFWOS Test #13. When adopted, fluid properties are evaluated at the same axial elevations for all the nodalization regions. In this way, the density difference, that is the natural circulation driving force, is properly evaluated avoiding an error source on the simulation outcomes (Mascari et al., 2011). Each pipe component is divided in twenty-six Control Volumes (CV), except the ones related to reflector assemblies in rows 8B and 9 (25 CVs) and the GEMs (20 CVs). For the first, the inlet nozzle was shorter since these assemblies were allocated within the inner radial shield support, as previously discussed. For the second, the top of the expansion volume, that is the fluid domain of interest for the hydraulic model, is below the assembly top by 0.806 m. It is important to note that the sodium/argon interface present in each GEM was included in the RELAP5-3D® input deck and simulated. For the reactor initial steady-state condition the sodium free level within these SAs was provided by the benchmark specifications (see Table 1). Flow areas and equivalent diameters were calculated for each assembly type and axial region along the coolant flow path (i.e., inlet nozzle, shield orifice region, absorber region, fuel bundle, reflector region, handling socket). The selected vertical nodalization adopted for each assembly type is provided in Fig. 4. In the figure, it is also possible to understand the correspondence between the RELAP5-3D® CVs and the SA axial regions, differentiated for each assembly type.

To properly assess the core pressure drops, the Cheng & Todreas model (1986) was adopted where a wire-wrapped hexagonal rod bundle is present (i.e., DFAs and CRs). RELAP5-3D® allows the user to modify the standard wall friction correlation to account for a more suitable correlation (The RELAP5-3D© Code Development Team, 2015b). The implementing procedure is discussed in detail in Narcisi et al. (2021). Each SA is provided with a shield orifice region, needed to obtain the desired core gagging scheme. The orifice geometry was available for each assembly type, while the associated minor head loss only for the DFAs (Sumner, 2018). In the RELAP5-3D® input deck, the orifices are simulated with Reynolds-independent concentrated k-loss coefficients. Their values, differentiated for each assembly type, were calibrated

CV#	Mesh H. [m]	DFAs	CRs/SRs	REFL. 7/8A	REFL. 8B/9	GEMs
26	0.1260	HANDLING SOCKET	HANDLING SOCKET	HANDLING SOCKET	HANDLING SOCKET	
25	0.1260	HANDLING SOCKET	HANDLING SOCKET	HANDLING SOCKET	HANDLING SOCKET	
24	0.1290	TOP END CAP		TOP ADAPT. BLOCK	TOP ADAPT. BLOCK	
23	0.1290	PLENUM SPACER	SHAFT	UPPER SHIELD	UPPER SHIELD	EXPANSION VOLUME
22	0.1290	PLENUM SPACER	SHAFT	UPPER SHIELD	UPPER SHIELD	EXPANSION VOLUME
21	0.1290	PLENUM SPACER	SHAFT	UPPER SHIELD	UPPER SHIELD	EXPANSION VOLUME
20	0.1290	PLENUM SPACER	SHAFT	UPPER SHIELD	UPPER SHIELD	EXPANSION VOLUME
19	0.1290	PLENUM SPACER	SHAFT	UPPER SHIELD	UPPER SHIELD	EXPANSION VOLUME
18	0.1290	PLENUM SPACER	TOP END CAP	UPPER SHIELD	UPPER SHIELD	EXPANSION VOLUME
17	0.1290	PLENUM SPACER	GAS CAPSULE SPRING	UPPER SHIELD	UPPER SHIELD	EXPANSION VOLUME
16	0.1266	PLENUM SPACER	GAS CAPSULE SPRING	CORE LOAD PAD	CORE LOAD PAD	EXPANSION VOLUME
15	0.1266	UPPER AX. REFL.	TOP SPACER			EXPANSION VOLUME
14	0.1524	FUEL PELLETS	ABSORBER	REFLECTOR	REFLECTOR	EXPANSION VOLUME
13	0.1524	FUEL PELLETS	ABSORBER	REFLECTOR	REFLECTOR	EXPANSION VOLUME
12	0.1524	FUEL PELLETS	ABSORBER	REFLECTOR	REFLECTOR	EXPANSION VOLUME
11	0.1524	FUEL PELLETS	ABSORBER	REFLECTOR	REFLECTOR	EXPANSION VOLUME
10	0.1524	FUEL PELLETS	ABSORBER	REFLECTOR	REFLECTOR	EXPANSION VOLUME
9	0.1524	FUEL PELLETS	ABSORBER	REFLECTOR	REFLECTOR	EXPANSION VOLUME
8	0.1348	LOWER AX. REFL.	LOWER SPACER	REFLECTOR	REFLECTOR	EXPANSION VOLUME
7	0.1348	BOTTOM END CAP	BOTTOM END CAP	LOW ADAPT. BLOCK	LOW ADAPT. BLOCK	EXPANSION VOLUME
6	0.1588	SHIELD ORIFICE REGION	SHIELD ORIFICE REGION	SHIELD ORIFICE REGION	SHIELD ORIFICE REGION	EXPANSION VOLUME
5	0.1227	SHIELD ORIFICE REGION	SHIELD ORIFICE REGION	SHIELD ORIFICE REGION	SHIELD ORIFICE REGION	EXPANSION VOLUME
4	0.1227	SHIELD ORIFICE REGION	SHIELD ORIFICE REGION	SHIELD ORIFICE REGION	SHIELD ORIFICE REGION	EXPANSION VOLUME
3	0.1397	SHIELD ORIFICE REGION	SHIELD ORIFICE REGION	SHIELD ORIFICE REGION	INLET NOZZLE	SH. OR. REGION
2	0.1238	INLET NOZZLE	INLET NOZZLE	INLET NOZZLE	INLET NOZZLE	INLET NOZZLE
1	0.1238	INLET NOZZLE	INLET NOZZLE	INLET NOZZLE	INLET NOZZLE	INLET NOZZLE

Fig. 4. RELAP5-3D© model of the FFTF core: correspondence between the selected vertical nodalization and the axial regions characterizing each assembly type, DFAs, CRs/SRs, REFL rows 7 and 8a, REFL rows 8b and 9, GEMs.

based on mass flow rate data and DFA dynamic pressure drops provided by benchmark specifications in nominal steady-state condition (Sumner, 2018). Iterative steady-state hydraulic calculations were run to reach this goal.

Several Heat Structure (HS) components are included in the model, accomplishing different functions for each assembly type. They simulate: i) the internal power source (either imposed as boundary condition or provided by the solution of the NK problem performed by the PHISICS code); ii) the thermal transfer within the assembly (e.g., pin/coolant within the DFAs); iii) the heat exchange between assembly and core bypass. They are also used to account for the material inventories (e.g., fuel, absorber, steel, and Inconel). Regarding the
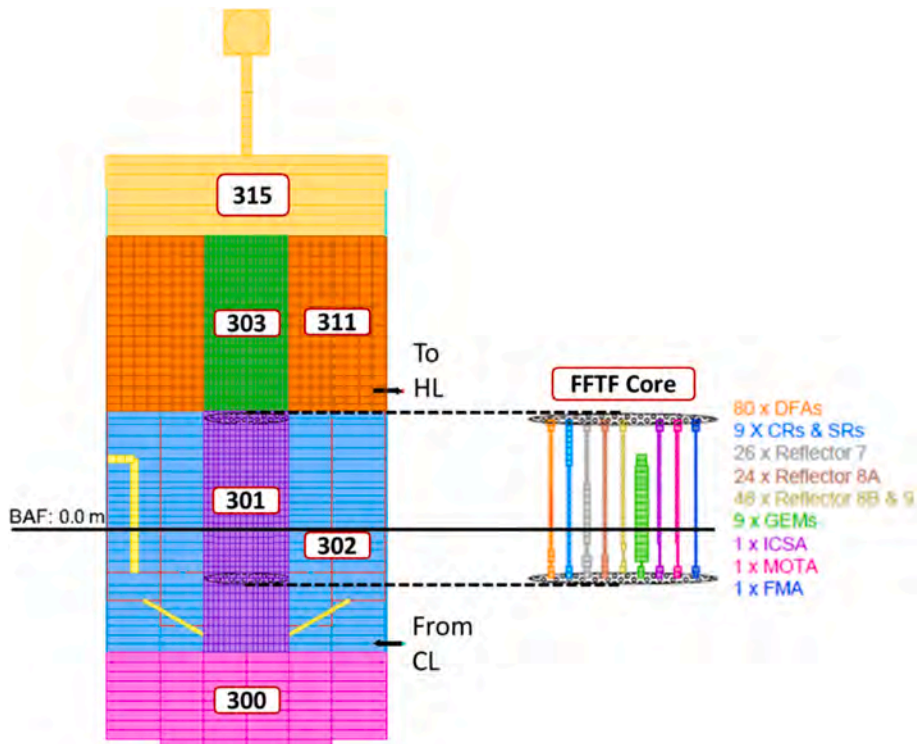

Fig. 5. RELAP5-3D© model of the FFTF RV: overview of the axial and radial nodalization associated with the MULTID components.

evaluation of the heat transfer coefficient, standard RELAP5-3D® liquid metal correlations are adopted: Seban & Shimazaki (1951) and Westinghouse (Kazimi & Carelli, 1976) correlations for non-bundle and bundle geometries, respectively.

3.1.2. RV model

The FFTF RV is simulated thanks to several MULTI-Dimensional (MULTID) components, whose nodalization is shown in Fig. 5. The MULTID component has been included in the latest versions of RELAP5 code series, such as RELAP5-3D®, to reproduce volumes where the fluid flow path is mainly mono-dimensional (e.g., core bypass, RV downcomer, etc.). The suitability of this component to model large plena was investigated and assessed by NERG in several computational campaigns (Narcisi et al., 2019, 2020a,2020b). For each CV, the MULTID component allows to consider three directions. For the present work, cylindrical geometry was selected (r, θ, z). The same azimuthal discretization was adopted for all the MULTID components. Six angular intervals, each one corresponding to 60°, were considered. The choice was driven by the actual geometrical symmetry of the reactor vessel. The axial division was developed according to the sliced approach, intensifying the CV number in the core active region to obtain more accurate results. In addition, to homogenize the mesh, the ratio between the length of two adjacent control volumes was limited below 1.25. Finally, a specific radial discretization was chosen per each MULTID component. The selected three-dimensional nodalization for the FFTF RV is summarized in Table 3.

Component #300 simulates the inlet plenum (pink in Fig. 5). The actual shape of the component is reproduced in the input deck calibrating the MULTID "volume factors". This user-defined parameter must be specified for each CV belonging to the MULTID. It is defined as the ratio between the actual volume and the original cylindrical volume (computed for each mesh starting from its position in the MULTID). This corrective factor is thus used to account for eventual empty spaces or something that takes up space inside the mesh volume, e.g., solid materials (fuel pins, structural materials, piping, etc.). This approach allows to reproduce the actual volume of the RV lower head (torospherical). In addition, to complete the MULTID input deck, "flow area factors" must be inserted for all the junctions belonging to the component. They are defined similarly to the "volume factor", as the ratio between the actual flow area and the original cylindrical flow area (computed considering the mesh position within the MULTID). This parameter allows to account for obstacles and to exclude some control volumes from the computational domains. To do so, each junction connected to the considered CV must be characterized by a null "flow area factor".

Component #301 models the central part of the RV (purple in Fig. 5). It is constituted by several components, axially located one above the other. In particular, the lower plenum of the core support structure, the core basket, and the core bypass. With respect to the model described in

Narcisi et al. (2021), the radial discretization was upgraded. This necessity was highlighted by the preliminary TH results. They are recalled in Fig. 6 and compared with the corresponding experimental data. The figure shows the core outlet temperatures associated with row 2 and row 6 PIOTAs. It can be noted that a similar trend was computed by the system code for both assemblies. Although, the experimental curves are quite different. The first peak (at nearly 9 s) is commonly experienced by the two components. Instead, the second one (whose time duration is higher) is detectable only for row 2 PIOTA. In the other, the temperature excursion is softer, and an almost flat plateau is present before the component cooling in the long-term. The different PIOTA behavior can be only partially explained due to the radial power distribution. Although, a significant role is also played by the heat transfer with the core bypass. Many studies in literature investigated this contribution (Wang et al., 2021; Moisseytsev & Sumner, 2022; Zhou et al., 2023; Hong et al., 2024; Hamase et al., 2024). It was recognized that the different PIOTA positions in the core could explain the dissimilarities acquired by the fast response TCs. PIOTA row 2 is in the core center, surrounded by other DFAs. The temperature axial profiles characterizing these assemblies are quite similar, producing a flat bypass temperature distribution in the correspondent region. This strongly reduces the assembly-to-bypass heat transfer. Instead, PIOTA row 6 is located near non-fuel assemblies (i.e., reflectors and GEMs). In this region, the bypass temperature experiences a relevant gradient, provoking a significant assembly-to-bypass heat transfer. To properly reproduce this phenomenon, a detailed nodalization of the core bypass is needed, accounting for the differences related to each radial region. For this reason, component #301 was updated, increasing the number of radii, and associating one of them to each core row (compare Fig. 7a with Fig. 7b). In addition, the model simulating the thermal coupling between bypass and assemblies was upgraded. The detail of the new methodology is shown in Fig. 7c. The hexagonal duct associated with each assembly (named A_1 in Fig. 7c) is decomposed in six edges. For each edge, a dedicated HS is used to represent the heat transfer between the sodium within the assembly and the proper MULTID #301 CV (in terms of radius and theta, see Fig. 7c). Convective boundary conditions are used for both left and right sides of the HS. This approach is replicated for all the axial thermal nodes and the core assemblies. As for the previous MULTID component, the volume occupied by the structural materials and the assemblies was excluded using calibrated "volume factors". Moreover, junctions "flow area factors" was computed to simulate the eventual sodium flow path in radial and azimuthal directions.
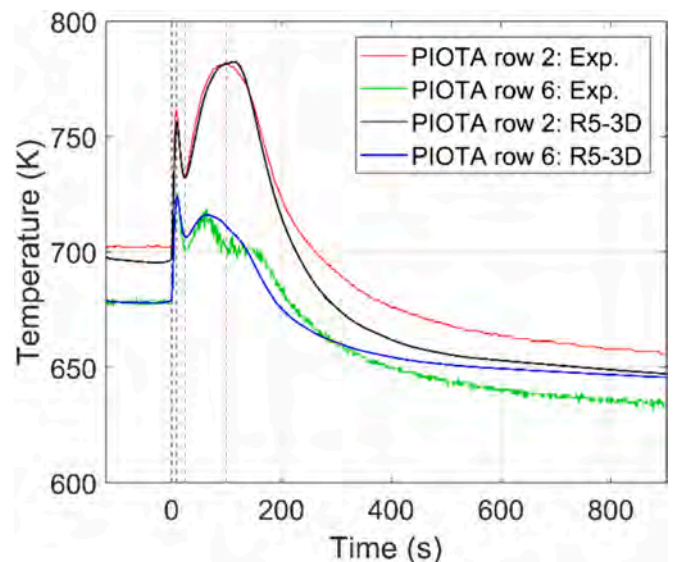
Table 3
RELAP5-3D© model of the FFTF RV: nodalization associated with the MULTID components.

Description	RELAP5-3D© ID	Radial Mesh N°	Azimuthal Mesh N°	Axial Mesh N°	Total CVs
Inlet Plenum	300	3	6	10	180
Lower plenum, Core basket, Core bypass	301	8	6	36	1728
Annular region between RV and core	302	3	6	27	486
Outlet Plenum – Above core	303	8	6	18	864
Outlet Plenum – Annular region	311	9	6	18	972
Total	–	–	–	–	**4230**

Fig. 6. Preliminary TH results (Narcisi et al., 2021): PIOTA row 2 and 6 outlet temperatures.
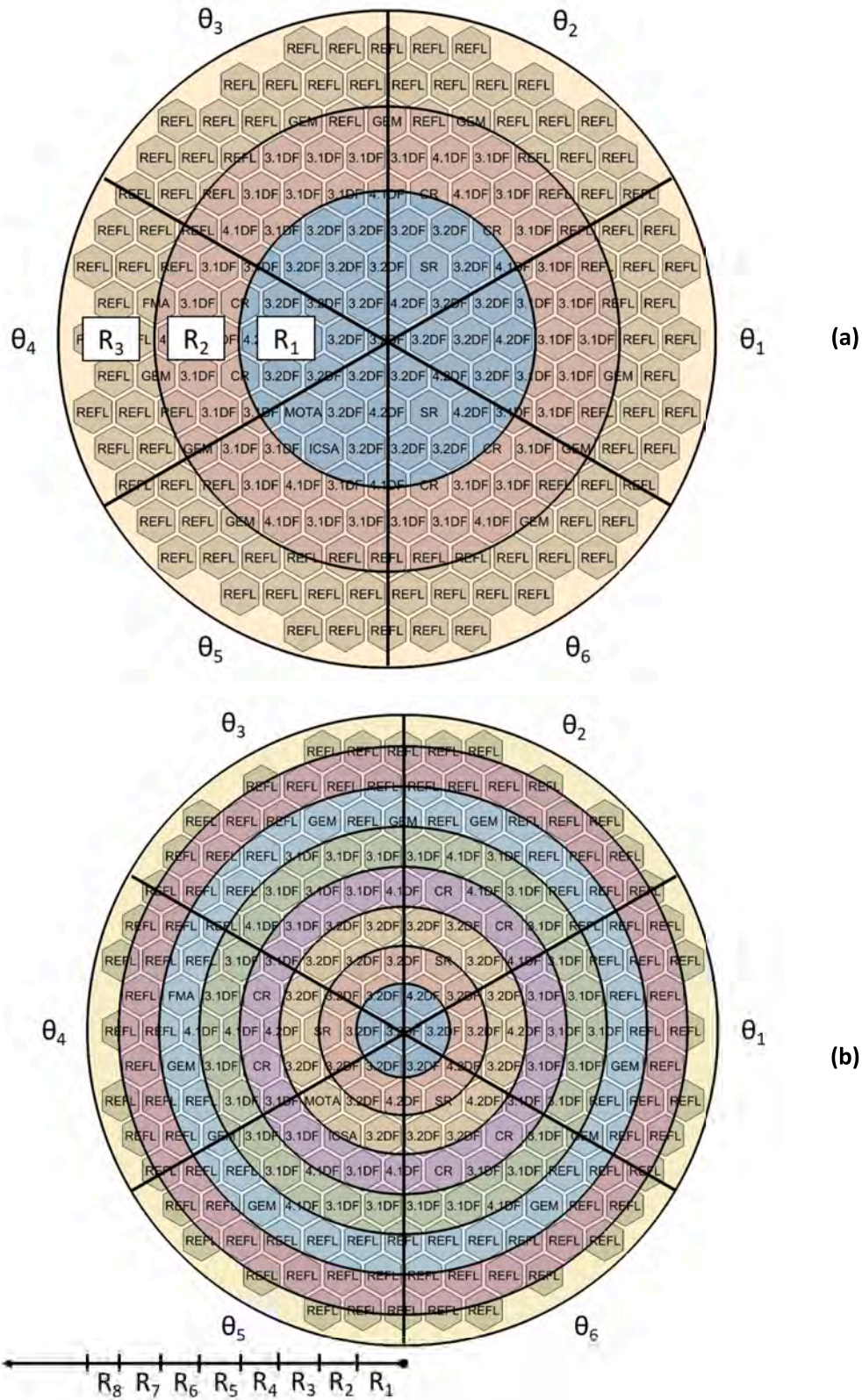
Fig. 7. RELAP5-3D© model of the FFTF core bypass: old mesh (a, Narcisi et al., 2021) and new mesh (b, used for open phase results). For the latter, the detail of the assembly-to-bypass thermal coupling is shown in (c). For the generic assembly A_1, the hexagonal duct is decomposed in edges. Each one couples the sodium within the assembly with the proper bypass CV (in terms of radius, R, and theta, θ). This methodology is repeated for all the axial thermal nodes and the core assemblies.
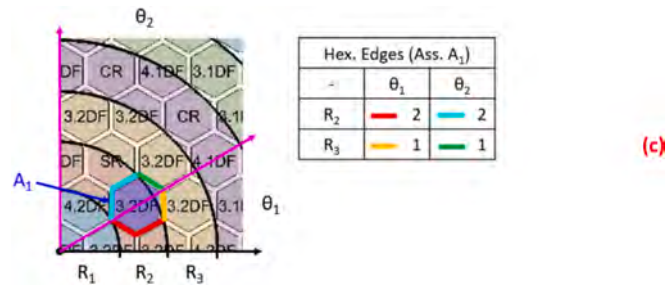
Fig. 7. (*continued*).

Component #302 reproduces the annular region between the core region and the reactor vessel walls (light blue in Fig. 5). The radial discretization was chosen considering the RV geometry. The first radius is associated with the region between the outermost SA row and the core barrel, where the radial shield is installed. The second radius contains the volume between the core barrel and the vessel thermal liner. The third radius simulates the bypass vessel cooling system. The channels connecting the lower and the lateral plena of the core support structure (see Fig. 1) are simulated with dedicated pipe components. Three additional pipe components are included to model the bypass coolant piping. For component #302, "volume factors" and "flow area factors" were calculated to consider the presence of the RV internals and to correctly simulate the sodium flow path within the CSS.

Component #303 (green in Fig. 5) and Component #311 (orange in Fig. 5) simulate the outlet plenum, between the horizontal baffle and the region just below the free level. The nodalization associated with this region was frozen after sensitivity studies. Both the radial and axial

mesh numbers were varied and their influence on the simulation results was evaluated. Increasing the vertical nodes had no significant impact on the numerical outcomes, as discussed in Narcisi et al. (2021). The selected average value for the axial mesh is 200 mm. Instead, the radial nodes number significantly influences the calculation results, above all for what concerns the prediction of the thermal stratification in the long term. This aspect is widely pointed out by studies present in literature (Wang et al., 2021; Zhou et al., 2023; Hong et al., 2024; Hamase et al., 2024). For this, the radial discretization of the RV outlet plenum was updated with respect to the one presented in Narcisi et al. (2021). Component #303 was used to model only the radial region above the core, adopting the same radial nodalization of the component #301 (see Table 3). In addition, a further MULTID component was introduced (#311) to reproduce the external annular region extending up to the RV inner wall. Open phase calculations were carried out with this new model. The division of the outlet plenum in two MULTID components is an arbitrary choice of the authors (mainly driven by post-processing
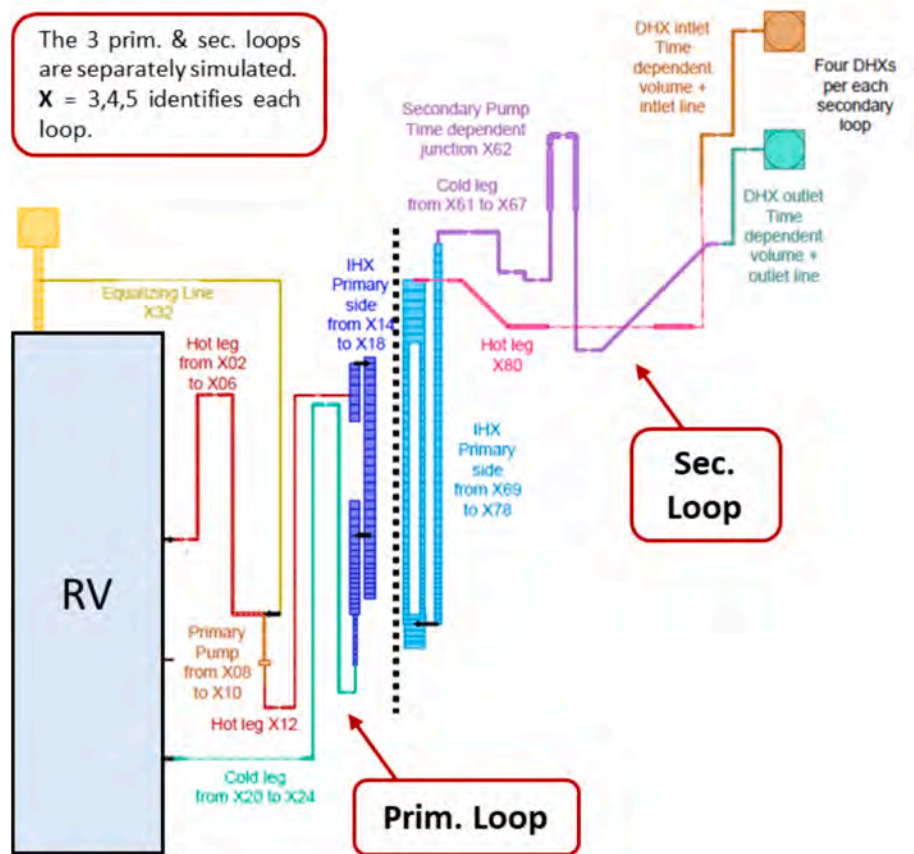

Fig. 8. Overview of the RELAP5-3D© model of the FFTF HTS.

needs). The same results can be achieved with a single component covering all the region radial extension.

The RV modelling is completed with a pipe component (#315, yellow in Fig. 5) simulating the argon cover gas.

3.1.3. HTS model

The Heat Transport System consists of three primary loops and three secondary loops. Each circuit is modelled in a separate way by using dedicated RELAP5-3D© one-dimensional components (e.g., pipes, branches, and pumps). The nodalization scheme of a single loop (including both primary and secondary circuits) is shown in Fig. 8. The primary loop nodalization includes the hot leg, the pumping system, the IHX primary side and the cold leg. The primary pumps are simulated with RELAP5-3D© pump components. For them, the implemented homologous curves were derived from the benchmark specifications (Sumner, 2018). The secondary loop input deck simulates all the related circuit except for the dump heat exchangers. The sodium thermodynamic conditions at the DHX inlet and outlet sections, i.e., outlet temperature and inlet pressure, are imposed as boundary conditions. The secondary loop nodalization scheme collects the cold leg, the secondary pump system, the secondary side of the IHX and the hot leg. The secondary pumps are simulated with time-dependent junctions, which set the correspondent flow rates. Referring to the IHX, the tube bundle is simulated with two ascending parallel pipe components, each one accounting for half bundle. Several heat structures simulate the thermal exchange occurring within the IHXs. It is important to note that the benchmark specifications do not provide any indication about the more appropriate HTC correlation to be used in the different heat transfer regions (i.e., core, IHX bundle, piping, etc.). The choice is up to the participants. Since the tube bundle is characterized by a high pitch-to-diameter ratio (nearly 1.5), the Graber-Rieger correlation modified by Sha and Launder (1979) is more appropriate to evaluate the shell side sodium heat transfer coefficient. The procedure to implement such expression within the input deck is described in Narcisi et al. (2020a). Instead, within the tubes, Seban & Shimazaki (1951) correlation is adopted. IHX HSs are also used to account for the component steel inventory as well as to simulate the heat losses towards the environment. Referring to the circuit pressure drops, the distributed head losses are evaluated by using the standard RELAP5-3D© wall friction correlation (Zigrang & Sylvester, 1985). Local pressure losses are simulated with concentrated k-coefficients, evaluated based on the actual geometries and the formulas available in Idelchik (1986). Pipeline thermal insulation is simulated for all the circuits by means of HSs, imposing the external surface boundary conditions (i.e., air temperature and HTC) indicated in the benchmark documentation (Sumner, 2018). To account for the delay introduced by the RTDs (see section 2.2), specific heat structures were connected to the hydrodynamic volumes corresponding to the HTS points where empirical acquisitions were performed. They simulate the series of a 2 mm external layer of AISI 316, a contact resistance of 5×10^{-4} m^2K/W and a 1 cm internal thickness of Al_2O_3. The temperature considered for the comparison with experimental data is the RTD innermost one (at the end of Al_2O_3 thickness). The adopted thicknesses, the chosen contact resistance and the thermal properties implemented for Al_2O_3 were derived from commercial datasheets (since they are not provided by the benchmark specifications).

3.2. Stand-alone TH calculations

During the benchmark open phase, as suggested by the organizers, a two-step methodology was followed. Firstly, calculations were carried out by imposing the reactor power as boundary condition and focusing on the FFTF thermal–hydraulic behavior. Then, they were repeated by using a coupled approach, to separately evaluate the impact on the numerical results of the NK phenomena.

Referring to the stand-alone TH model, a steady-state calculation was run to validate the prepared input deck and to fully characterize the

FFTF reactor initial conditions. The core NK power distribution in this state was provided by the benchmark specifications (Sumner, 2018). Hydraulic tests were performed with the input deck to match the core gagging scheme indicated in the benchmark specifications, as well as the reference pressure drops related to the DFAs. The concentrated k-loss coefficient associated with the shield orifice region was tuned for all the assembly types to fulfil this scope. For each group of assemblies, the mass flow mean value, the relative standard deviation (σ%) and the relative difference (Δ%) between the calculated mean value and the benchmark specification data were computed. The calibration process was iteratively carried on until all the σ% and the Δ% were below 0.1 % and 1 %, respectively. Finally, further hydraulic tests were performed to tune the loop pressure drops (e.g., piping, IHXs, etc.) and align them to the data provided in the benchmark specifications (Sumner, 2018).

Starting from this reactor initial state a transient simulation involving the LOFWOS Test #13 was run. For calculation purposes, time trends were set for the following boundary conditions: primary pumps speed, secondary loop mass flows, temperatures at DHXs outlet, and total reactor power. For what concerns the latter, in first approximation, it was distributed between the core assemblies according to the radial distribution present at the initial state (and provided by the benchmark specifications). It was postulated that the power map is not jeopardized during the accidental evolution. This was considered a reasonable assumption since the LOFWOS Test #13 is a symmetrical transient (all primary pumps are shut down) and the core loading scheme is also nearly symmetrical. This aspect was even confirmed by the following TH/NK coupled simulations. Transient analysis was performed with a time step of 5×10^{-3} s. A time step sensitivity analysis, ranging from 5×10^{-3} s to 5×10^{-4} s demonstrated the independence of the calculation outcomes from this parameter. The selected figures of merits to perform the comparison between numerical outcomes and experimental data are: PIOTA row 2 & row 6 outlet temperatures; primary loop hot & cold leg temperatures; secondary loop hot & cold leg temperatures; primary loop mass flow rate. They are collected in Fig. 9. In the figure, the black solid lines represent the experimental data, the blue dashed lines the old results already presented in Narcisi et al. (2021), and, finally, the red dotted lines the refined numerical outcomes associated with the current work. The plotted quantities belong to the HTS loop one but the behavior of the other two loops is the same (symmetrical transient). For sake of brevity and clarity, these additional parameters, as well as their comparison with the simulation results, were not included in the plots of Fig. 9.

The first PhW consists in the two minutes before the Postulated Initiating Event (PIE). DHX fan speed is reduced, and secondary sodium temperature starts to rise at the component outlet. Considering the RTD thermal inertia significantly improves the agreement between the numerical outcomes and the experimental data. Looking at the secondary cold leg temperature (Fig. 9f), the anticipation present in the previous results is no more present (compare blue dashed and red dotted lines). Also, the parameter fluctuations are flattened, following better the shape of the experimental trend. Although, an overprediction of few degrees is still present. This difference cannot be justified with the heat losses related to the pipe section between the DHX outlet and the point of the experimental acquisition (downstream the pump). Indeed, their value, indicated in the benchmark specifications, is well below the magnitude of the deviation visible in Fig. 9f. This aspect remains an opening issue. This discrepancy propagates from secondary to primary circuit. Since IHX is a counterflow heat exchanger, the primary outlet temperature follows the secondary inlet one. Thus, a temperature difference of the same magnitude is also visible in the cold leg temperature (Fig. 9d), measured just downstream the IHX. This alteration is absorbed by the RV inlet plenum. Thus, it does not affect neither the core, as demonstrated by the PIOTA outlet temperatures (Fig. 9a/b), nor the hot section of the primary loop, as witnessed by the hot leg temperature (Fig. 9c). In the first PhW, the code provides a good estimation of these temperatures, with only small deviations with respect to the experimental data.
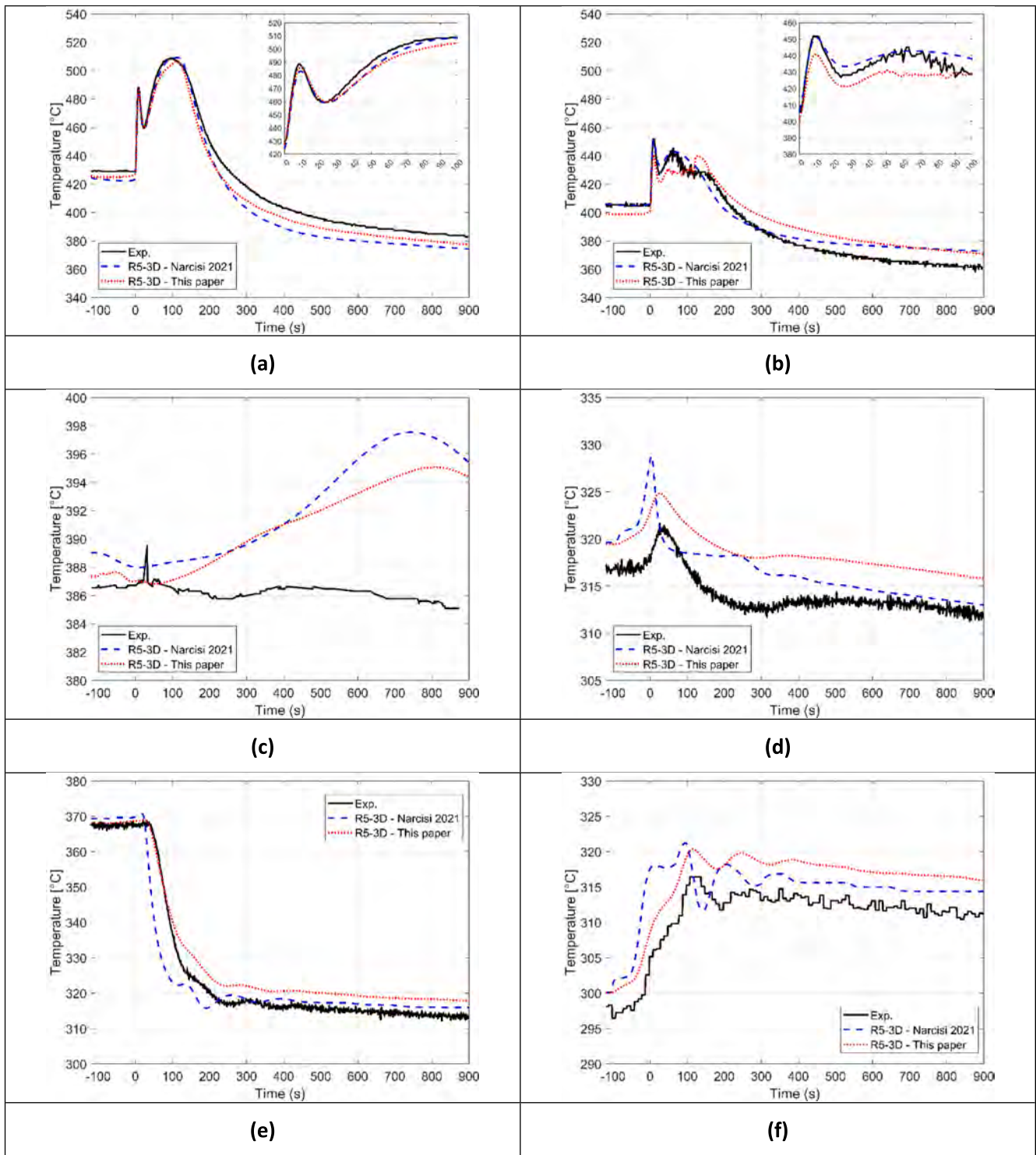
(a)

(b)

(c)

(d)

(e)

(f)

Fig. 9. FFTF LOFWOS Test #13, comparison between experimental data (black solid lines), old results already presented in Narcisi et al. (2021, blue dashed lines) and refined numerical results associated with this work (red dotted lines): PIOTA row 2 (a) and row 6 (b) outlet temperatures; primary loop hot (c) and cold (d) leg temperatures; secondary loop hot (e) and cold (f) leg temperatures; primary loop mass flow rate (g).

The second PhW starts with the PIE and terminates when the first peak in the PIOTA temperatures is reached (see Table 2). Experimentally, its extent corresponds to nearly 60 °C and 45 °C for PIOTA row 2 and row 6, reaching a maximum of 488 °C and 451 °C, respectively. The spike is very well reproduced for PIOTA row 2 (Fig. 9a), while it is slightly underestimated for row 6 component (Fig. 9b). This is partially due to a lower initial temperature (coming from PhW1). Considering

this bias, the temperature excursion is underestimated of only few degrees.

The third PhW is characterized by the power reduction driven by the negative reactivity feedbacks, i.e., Doppler effect, CR/SR axial dilatation and, above all, GEM sodium level drop (see section 2.2). During this time window, the mass flow decrease, due to the prosecution of the pump coast down, is well predicted by the code, as witnessed by Fig. 9g. PIOTA
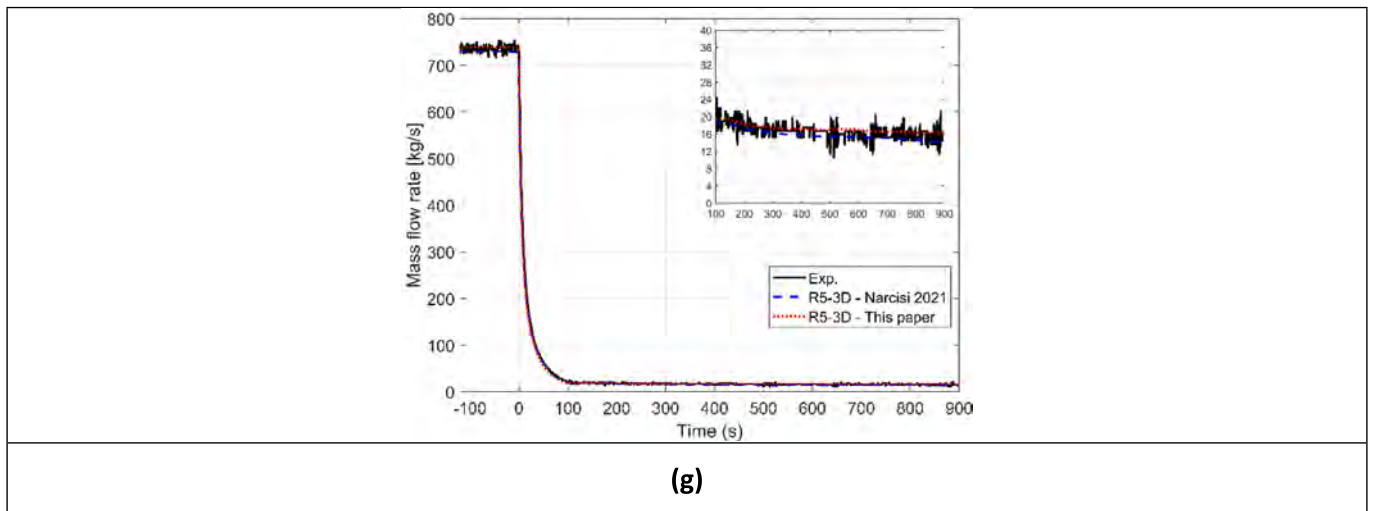
(g)

Fig. 9. (*continued*).

TCs experience a noticeable temperature decrease (Fig. 9a/b). This PhW is finely simulated by the code. For row 6 component, the temperature bias present at the end of PhW2 propagates also in PhW3 but the parameter excursion is precisely reproduced.

The fourth PhW begins when the GEM level moves below the BAF and concludes when natural circulation is completely established. Since the GEM negative contribution to the core reactivity is terminated, PIOTA outlet temperatures restart to rise. The two parameters are very satisfactorily evaluated (Fig. 9a/b). The introduction of a detailed nodalization for the core bypass allows to differentiate in an effective way the assembly-to-bypass heat transfer in the various radial regions and to properly reproduce the temperature plateau characterizing the PIOTA row 6 outlet temperature trend. This aspect deserves a wider discussion. The detail of the PIOTAs thermocouple probes is shown in Fig. 10 (Lucoff, 1989). They are installed within an adapter located just above the assembly outlet. This configuration allows to almost completely exclude the sodium coming out of the adjacent assemblies. In this way, the PIOTA measurements are not affected by mixing and deviation effects at the core outlet. The experimental data provided by the benchmark specifications are the mean of the three measurements placed around the probe center (see Fig. 10). If the hot sodium jet coming out from the assembly is characterized by a significant radial gradient, then the provided data do not coincide neither with the average nor with the maximum temperature in this jet, but rather with an intermediate value. Among the benchmark participants, a detailed analysis referred to this aspect was performed by the Commissariat à l'Énergie Atomique et aux Énergies Alternatives (CEA, Gerschenfeld et al., 2023) by using the multi-scale coupling code MATHYS. They demonstrated the need of simulating the PIOTAs sodium outlet jets with dedicated CFD calculations. Moreover, they identified a possible explanation to the PIOTA row 6 outlet temperature fluctuations in the turbulent jet oscillations. However, they conclude that the PIOTAs local measurements can be hardly related to the predictions of a STH code, due to the strong influence of complex 3D phenomena such as the radial heat transfer through the inter-wrapper region. For this, the result in Fig. 9b, obtained by using a very detailed model of the assembly-to-bypass heat transfer is a very satisfactory outcome. Focusing on the secondary loop, a large temperature decrease is experienced in the hot leg (Fig. 9e). This is due to the significant heat transfer reduction occurring within the IHXs. The decrease of the primary side mass flow produces a relevant drop of the correspondent velocity and heat transfer coefficient profiles that inhibits the thermal exchange. During blind
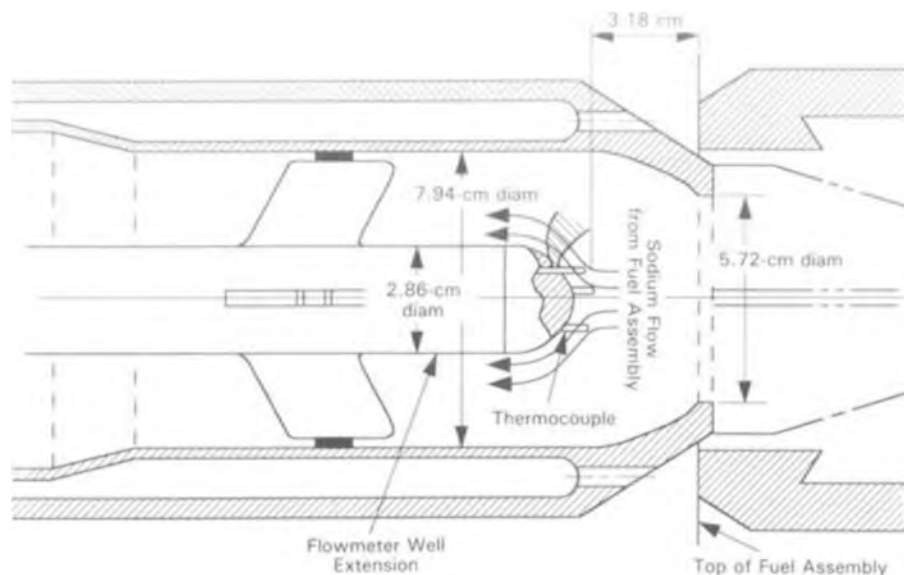

Fig. 10. Detail of the PIOTAs thermocouple probes (Lucoff, 1989).

phase, RELAP5-3D© predicted an anticipated reduction of the hot leg temperature (blue dashed line). The introduction of the RTD thermal inertia enhances the code modelling capabilities with respect to this parameter, allowing a correct simulation of the temperature drop (red dotted line). Nevertheless, an overprediction of the parameter values is visible in the mid-long term. This deviation is driven by the correspondent temperature increase experienced by the primary loop hot leg and discussed in the following.

The fifth PhW starts with the complete transition to natural circulation and lasts up to the End of Transient (EoT). Fig. 9g shows this moment, occurring nearly 100 s after the PIE. RELAP5-3D© well reproduces this phenomenon. Later, the measured mass flow experiences large fluctuations around the mean value, considerably higher than the flowmeter uncertainty band. However, a good agreement is found between the average experimental data and the simulation outcomes. PIOTA temperatures show a gradual decrease (Fig. 9a/b). For row 2 component, the difference between the numerical outcomes and the experimental data is of few degrees along the overall PhW. Instead, the difference is higher for row 6 PIOTA (around ten degrees). This can be explained in various ways. The most reasonable justification seems related to the calculation assumptions. Indeed, a constant k-loss coefficient is imposed to the shield orifice region associated to each assembly, even if they should be a function of the flow rate (i.e., Reynolds number). These concentrated pressure drops have been calibrated based on the initial condition data and they could strongly affect the flow distribution during low flow transient scenarios. Referring to the primary loop hot leg (Fig. 9c), numerical results agree with the experimental data up to nearly 100 s, when the temperature is kept almost constant thanks to the large thermal inertia of the RV outlet plenum. Later, TCs observe a small temperature decrease (nearly 1 °C). On the contrary, RELAP5-3D© predicts a temperature increase of few degrees reaching a peak (395 °C) nearly at EoT. Several phenomena affect the hot leg temperature, e.g., core outlet temperature, thermal stratification and mixing convection within RV outlet plenum, thermal inertia of the submerged solid structures, and heat losses. Unfortunately, the benchmark specifications do not provide the thermal–hydraulic data needed to fully characterize the sodium flow path going from the core outlet to the hot leg inlet, and this makes it difficult to identify the origin of such disagreement. Also, other benchmark participants obtained similar trends for this parameter (see Hong et al., 2024; Hamase et al., 2024). This deviation in the primary hot leg temperature is dampened by the IHX. Indeed, as mentioned above, the secondary hot leg temperature experiences a similar increase, as well as the IHX exchanged power. For this, the alteration does not propagate to the cold section of the primary loops. However, it is worth to be noted that the deviation is only of few degrees, thus, very little in percentage with respect to the overall primary system temperature difference.

Finally, Fig. 11 shows the RELAP5-3D© prediction of the sodium thermal pattern within the RV outlet plenum in some relevant moments of the LOFWOS Test #13. They were selected based on the PhWs listed in Table 2. The temperature contour was limited between 370 and 430 °C to better highlight the thermal phenomena occurring within the outlet pool during the test. Up to the PIE (Fig. 11a), hot sodium exits core assemblies, moves upwards in the central part of the plenum, mixes with the colder sodium, and returns downwards near the RV walls, where there are the hot leg connections. After PIE, scram command is not operated and the core outlet temperatures increase, warming up the central region of the outlet plenum. This enhances the sodium mixing in the first part of the transient (PhW2 to PhW4, corresponding to Fig. 11b/c/d). The RV upper region is heated with the formation of a slight thermal front, that progressively moves downwards (compare Fig. 11b/c/d) and reaches the bottom of the outlet pool at around 300 s after the PIE (Fig. 11e). At this point, the core outlet temperature becomes colder than the one of the outlet plenum, and the sodium flow is limited to the bottom region. The upper region of the outlet plenum is not interested by the flow path, promoting the establishment of a thermal stratification

just above the hot leg connections (Fig. 11f). A thermal front of about 20 °C is predicted by the code. This transient evolution is confirmed by the outcomes obtained by other benchmark participants (Wang et al., 2021; Zhou et al., 2023; Hong et al., 2024).

3.3. NK model

Since 2011, PHISICS (Parallel and Highly Innovative Simulation INL Code System, Alfonsi et al., 2019) has been integrated within RELAP5-3D© as the toolkit called to solve the NK problem. For this purpose, the internal coupling structure shown in Fig. 12 is adopted. PHISICS relies on a nodal solver, called INSTANT, to compute the second order formulation of the transport equation in any user-input number of energy groups. The self-shielded macroscopic cross sections needed as input terms in the transport equation are linearly interpolated for all the core materials starting from a N-dimensional Cartesian grid. Its dimensions are core TH parameters, such as fuel and coolant temperature, coolant density or boron concentration. No limits are foreseen for the tabulated dimensions and the points per dimension. The macroscopic cross sections associated with each grid point are computed by the cell/lattice calculation module (named ECCO) integrated in ERANOS code (Rimpault et al., 2002). Then, they are tabulated in a.xml file, given in input to the coupled simulation. At each time step, the TH input parameters for the PHISICS interpolation are provided by the solution of the TH problem performed by RELAP5-3D© code. Once interpolated, the macroscopic cross sections are used by INSTANT to solve the transport equation in each mesh of the NK nodalization. Finally, the axial/radial power map resulting from the solution of the transport equation is passed to RELAP5-3D© that uses these data as boundary conditions to re-solve the TH problem. This process constitutes the internal iteration performed by the coupled codes at each time step. Once the convergence is reached, the simulation advances in time. The PHISICS/RELAP5-3D© internal coupling structure also allows the user to differentiate the time steps of the NK and TH problems, to speed up the simulations.

For the purposes of FFTF NK calculations, the following Cartesian grid dimensions were selected: fuel temperature (two points, 300 and 2000 °C), coolant temperature (two points, 300 and 600 °C), control rod position (two points, "inserted" and"not inserted") and coolant density (three points, 1.2, 860 and 1000 kg/m^3). Referring to the latter parameter, the first point was used to simulate the eventual presence of argon gas in the considered CV (e.g., in the GEMs). In this approach, the sodium within the GEM is treated as the two-phase water in the Boiling Water Reactors (BWR). The temperature tabulation is adopted to evaluate the liquid sodium properties, while the density coefficient to model the effect of the level decrease. Indeed, in each CV, the mixture density calculated by RELAP5-3D© is used to interpolate between the thermal properties belonging to the liquid sodium and the Argon cover gas. The grid point-associated cross sections were computed by ECCO cell code, by setting 15 energy groups and the P1 approximation for scattering treatment. In addition, thermal expansion and Doppler effect were evaluated for all the core materials. Referring to the former, the radial expansion of the inter-assembly gap is controlled by the coolant temperature. Since only two values are considered, see above, the resulting dilatation is linear. This corresponds to a simplified 'free' flowering effect. Considering the more articulated geometry of the FFTF core restraint system (e.g., the presence of the above core load pads) the expected thermomechanical response is more complex. Thus, the adopted approach introduces a simplification whose effect on the simulation results will be analyzed in the next section. The material compositions needed for simulation purposes were derived from benchmark specifications (Sumner, 2018). Since the LOFWOS Test #13 was not performed at the beginning of a cycle, all the DFAs had a slightly different material isotopic composition within the core active region (see Fig. 4). For each DFA, the latter was divided in eight axial zones, two containing the bottom and top insulator pellets and six referred to
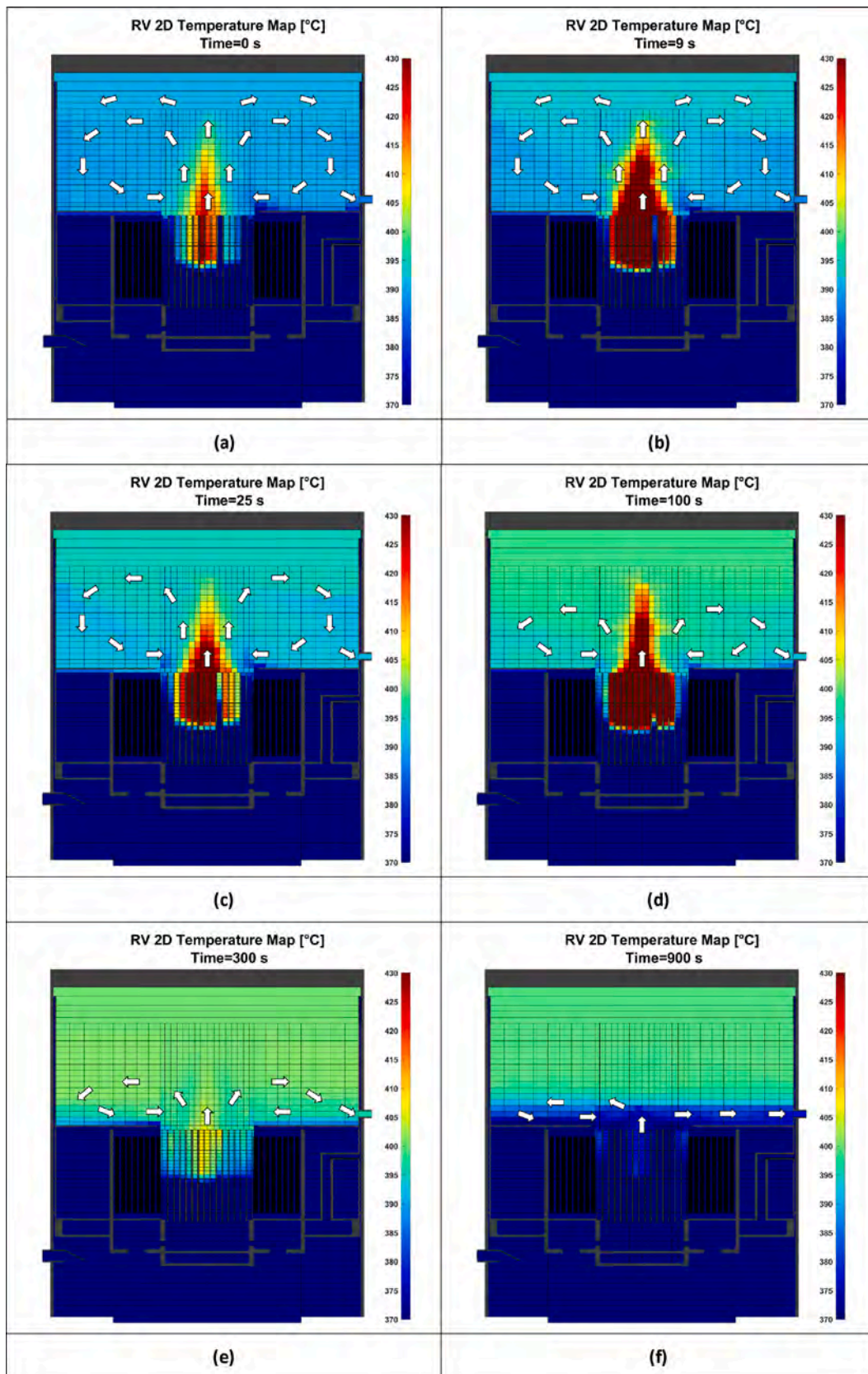
Fig. 11. FFTF LOFWOS Test #13: sodium temperature map within the RV throughout the transient evolution.
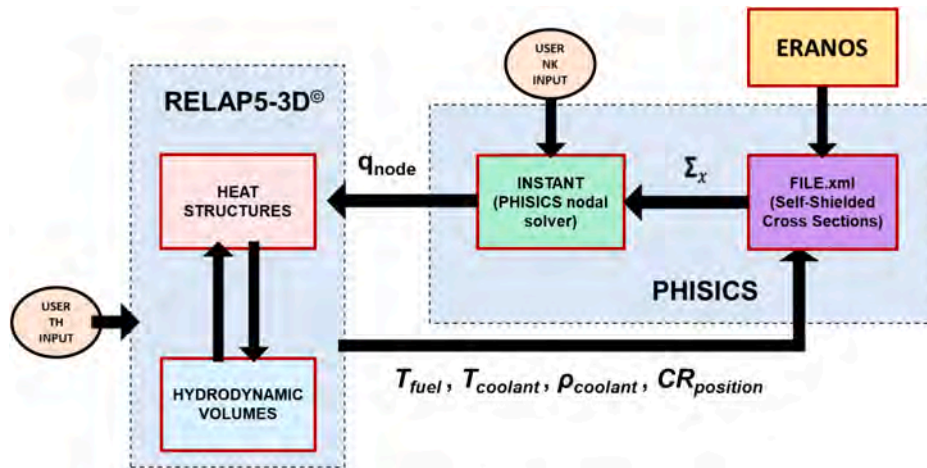
Fig. 12. PHISICS/RELAP5-3D©: coupling structure.

the fuel pellets, for a total of 640 materials (i.e., 80 assemblies per 8 axial zones). Four additional material compositions were provided to characterize the DFAs shield orifice region, lower and upper axial reflectors and plenum spacer (see Fig. 4). In this case, they are in common for all the DFAs. Finally, thirty other material compositions were reported in the benchmark specifications to fully describe the other core assemblies (i.e., CRs, SRs, radial reflector, GEMs, ICSA, MOTA, FMA) and the outermost radial shield. All the indicated materials (i.e., 674) were included in the TH/NK coupled model. The JEFF 3.1.1 nuclear data library was considered by ECCO. The PHISICS NK nodalization foresees 30 axial meshes, including all the core axial regions except for the inlet nozzle and the handling socket. With respect to the vertical discretization in Fig. 4, used for the TH model, the mesh number was doubled between the DFA lower and upper axial reflectors (coinciding with CVs 8–15 in Fig. 4). This improved the simulation results and was the outcome of a sensitivity study on the NK mesh number. Radially, a NK node was associated with each core assembly. The total number of NK nodes is 5970 (i.e., 199 assemblies per 30 axial meshes). Zero flux boundary conditions were used to close the NK problem at the core edges. At each time step, the NK convergence criteria are: 1 pcm for the k-effective value and 1.0×10^{-4} for the neutron flux, expressed in terms of the ratio between the values of two following iterations. For gamma power, the ANS05 curve with four isotopes is used (American Nuclear Society, 2005).

3.4. TH/NK coupled calculations

The simulation of the FFTF LOFWOS Test #13 was repeated by using the coupled codes. To reproduce the core initial state, the hydraulic settings discussed in the previous section were maintained. Thus, the core gagging scheme was also finely reproduced by the coupled calculation, as well as the core and loop pressure drops. In this case, the core NK power distribution was computed by PHISICS. The simulation results for the DFAs were compared with the data provided by the benchmark specifications, obtained by running a transport calculation with the PERSENT code (Sumner, 2018) and considering P3 approximation and both neutron power and gamma heating. For each assembly, the relative difference was evaluated and reported in Fig. 13a. The two datasets are in good agreement with relative deviations ranging from −2.5 % to + 5.5 %. Globally, PHISICS predicts a slightly more peaked NK power distribution with the DFAs power that exceeds the reference value of 2.7 %. The latter was computed as the relative difference between the sum of the DFAs power terms evaluated by PHISICS and the sum of the corresponding ones reported in the benchmark specifications. The resulting sodium temperatures at the core outlet are shown in Fig. 13b. The maximum of the distribution, circled in blue, corresponds to row 2 PIOTA (compare with the assembly position reported in Fig. 2).

Starting from this initial state, a transient calculation was performed. The selected figures of merit to assess the performances of the coupled codes are: the sodium temperatures at the outlet of row 2 and row 6 PIOTAs; the fission power and the decay heat produced within the core.
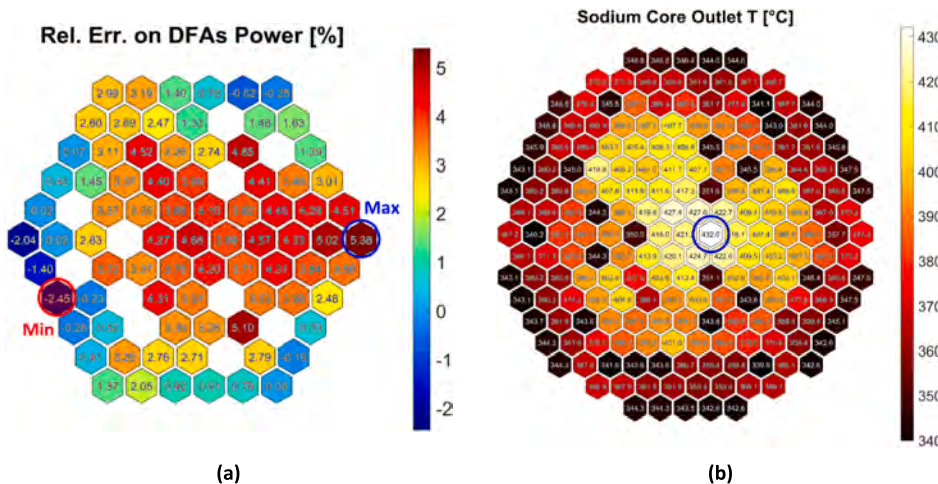

(a)

(b)

Fig. 13. FFTF LOFWOS Test #13, initial conditions: relative error on DFAs NK power (a) and radial distribution of sodium core outlet temperatures (b).
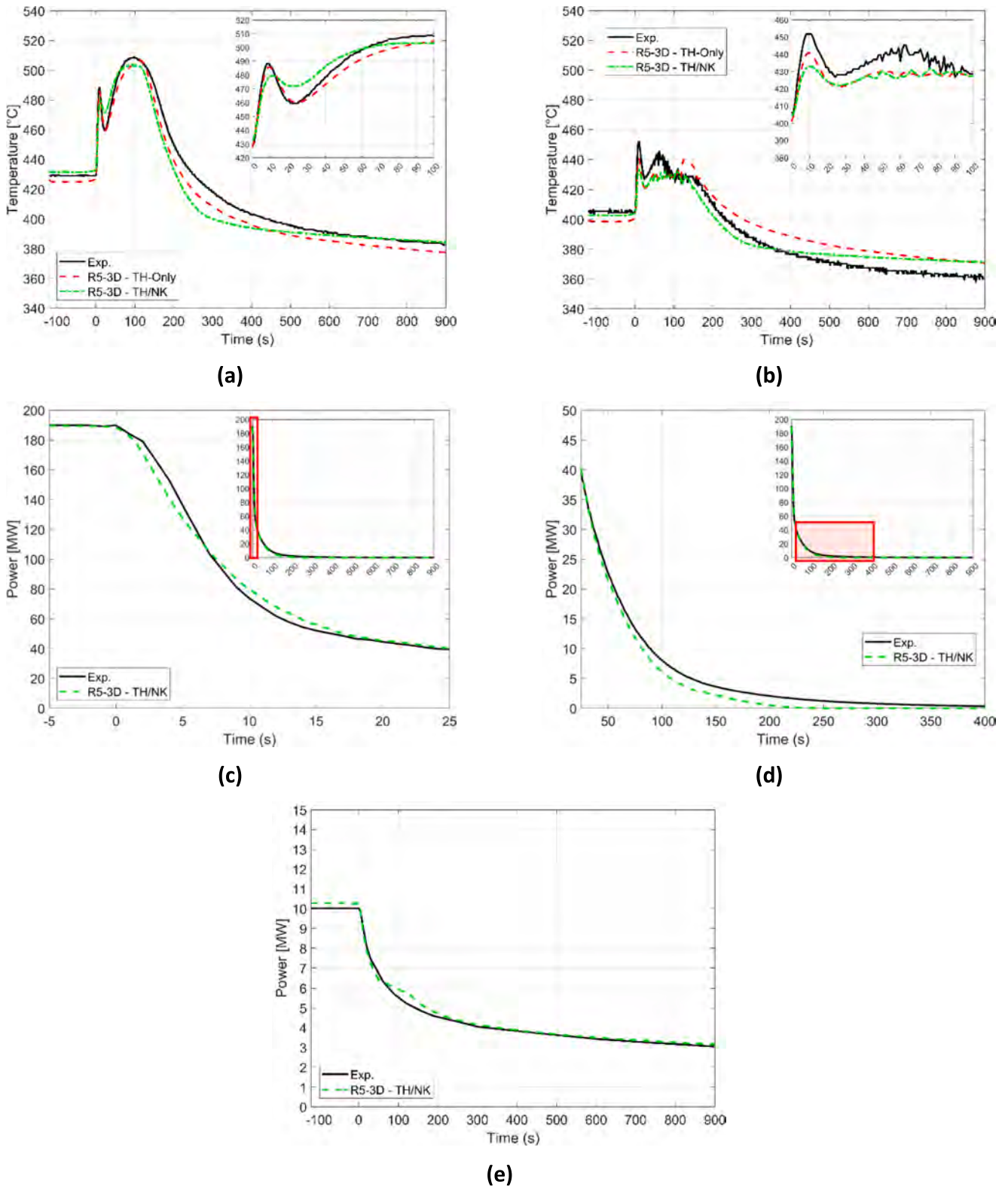
Fig. 14. FFTF LOFWOS Test #13, comparison between experimental data (black solid lines) and RELAP5-3D© results, TH-only (red dashed lines) and TH/NK (green dotted/dashed lines) calculations: PIOTA row 2 (a) and row 6 (b) outlet temperatures; Core fission power in the short term (c) and mid-term (d) and decay heat (e).

They are collected in Fig. 14. There, black solid lines represent the experimental data, while dashed lines reproduce the numerical results. Red and green colors are used for the TH-only and coupled simulations, respectively. Hydraulic parameters (e.g., primary mass flow) are not included, since nearly identical to the ones already discussed in the previous section.

previous section. More in general, the coupled codes results associated with the RV and the HTS are very similar to the ones referred to the TH-only simulation. This can be seen in Fig. 15, comparing the RV 2D sodium temperature maps for the two calculations. The selected time is 100 s, corresponding to the second and maximum peak in the core outlet
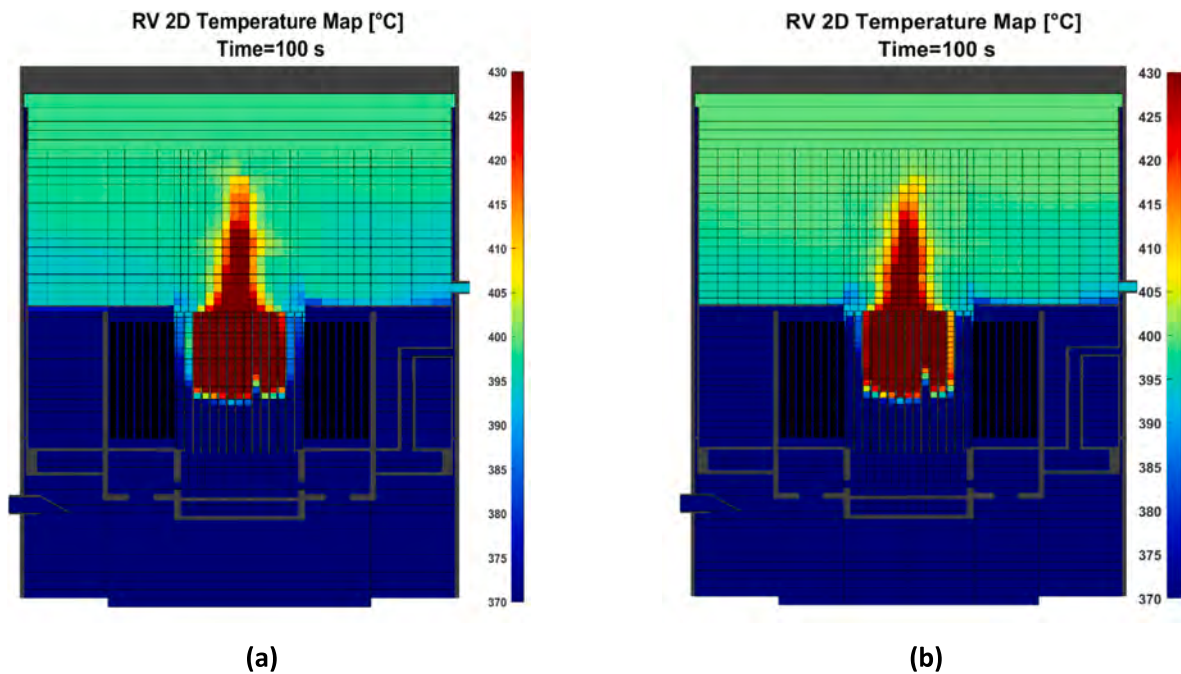
Fig. 15. FFTF LOFWOS Test #13: comparison between the sodium temperature maps within the RV obtained with the TH-only (a) and TH/NK (b) calculations. The selected time is 100 s, corresponding to the second and maximum peak in the core outlet temperature.

temperature (see Table 2). As visible, only small deviations can be detected, while the general trend of the physical phenomena occurring within the pool is the same. This is due to the fact that, even if some differences are present in the core TH/NK performances, their magnitude is reduced (as discussed in the next paragraphs) and, since they are local effects, they nearly disappear when averaged within the CVs belonging to the RV outlet plenum. Another experimental trend missing in Fig. 14 is the one related to the total reactor power. It was excluded for sake of brevity since it is the sum of the fission power and the decay heat. Thus, all the considerations done in the following for these two parameters can be also extended to it.

Referring to the FFTF core, during PhW1, the coupled codes are able to well reproduce the experimental data. This is expected since, during this time window, no significant NK alterations are introduced with respect to the initial state analyzed in the paragraph above and shown by Fig. 13a and b.

In the short term after PIE (PhW2 & PhW3), the numerical trend of the core fission power shows two main deviations with respect to the experimental data (Fig. 14c). In particular, the calculated power decreases slightly earlier and slower. This causes a first underprediction and a following overprediction, with a switch at around 7 s. These power mismatches correspondingly alter the shape of the PIOTAs outlet temperature trends (see the box in the top right corner of Fig. 14a and b). The first temperature peak is smoothed, as well as the following drop. This effect is more marked in the row 2 component where the power is higher, and the assembly-to-bypass heat transfer is lower. The first power deviation in Fig. 14c, i.e., the higher power negative derivative just after the PIE, is probably due to an overestimation of the reactivity feedback related to the fuel and clad temperatures. This can be due to the values assumed for the gap and the fuel conductance. In the future development of the activity a sensitivity study on these parameters will be conducted. Instead, the second power difference, i.e., the power overestimation after 7 s, is due to the GEM reactivity feedback. Indeed, in our simulation the level within these components lowers more slowly with respect to the theoretical curve suggested in the benchmark specifications (Sumner, 2018). This is probably related to the calculation assumptions. The most probable is the constant K-coefficient imposed at the assembly inlet to tune the TH model and obtain the reference core

gagging scheme. Future sensitivity studies will also involve this parameter. In addition, it is worth to remind that the thermal expansion feedbacks are linearly approximated when generating the self-shielded macroscopic cross sections with ECCO cell code, introducing another potential error source. Finally, it must be noted that a precise calculation of the different contributions to the total reactivity due to each feedback cannot be directly done in our case. Unfortunately, the part of the PHISICS code related to these evaluations has not yet been finalized and validated.

When referring to the mid-term (PhW4), PHISICS underpredicts the fission power (Fig. 14d). In this time window, the GEM reactivity feedback is no longer present and cannot be an error source. In this case, the power deviation is probably due to the absence of specific thermo-mechanical feedbacks, such as the ones related to the different elements of the core restraint system (i.e., diagrid, above core load pads, etc.). Indeed, as already pointed out, they are only globally included in the linear approximation used to generate the macroscopic cross sections. The power deficiency consequently leads to the underprediction of the PIOTAs outlet temperatures, starting from the second peak and characterizing the component mid-term behavior.

Finally, for what concerns the PhW5, the NK code provides a good estimation of the reactor decay heat (Fig. 14e). The long-term temperature of the row 2 PIOTA well agrees with the experimental data. Instead, for row 6 component, a deviation can be detected. However, it corresponds to the one already observed for the TH-only simulation. Thus, the origin is the same and the possible justifications have been already discussed in section 3.2.

A valid method to evaluate the modelling capabilities of the coupled codes with respect to the simulated transient is the one indicated in Prosek et al. (2002) and based on the fast Fourier transform (FFTBM). The methodology clearly indicates when simulation needs to be improved, showing the measurement–prediction discrepancies in the frequency domain. The acceptability factor for code calculation was determined based on several hundreds of code calculations. The FFTBM method has been applied to various international standard problems and other experiment simulations that are presented in Prosek et al. (2002). For sake of brevity, the details of the procedure are omitted in the following. What is important to underline is that, for each variable of

interest, this method allows to quantitative assess the agreement between the experimental trend and the numerical one. To fulfill this scope, the parameter accuracy, named AA_p, is defined as the sum of error function amplitudes normalized to the sum of experimental signal amplitudes:

$$AA_p = \frac{\sum_{n=0}^{2^m} |\widetilde{\Delta F}(f_n)|}{\sum_{n=0}^{2^m} |\widetilde{F_{exp}}(f_n)|}$$

where $\widetilde{F_{exp}}$ and $\widetilde{\Delta F}$ are the amplitudes of the experimental and error signals obtained with the FFT at the frequencies f_n, and n, going from 0 to 2^m, is the number of points defining the two functions in the time domain. Typically, m ranges between 8 and 11. To determine the needed n, the following relationship is suggested in Prosek et al. (2002), based on the sampling theorem.

$$2f_{max} = \frac{2^{m+1}}{T_d}$$

where T_d is the considered transient time window, and f_{max} is the highest (maximum) frequency component of the signals. Thus, the FFTBM application implies the selection of a time window, of a maximum frequency and of a cut-off frequency (f_d). The latter is the frequency beyond which the amplitudes are not accounted when calculating the AA_p values. It deserves to cut off spurious contributions due to high frequencies, generally negligible. For the current application, T_d was chosen equals to the transient duration (i.e., 1020 s, see Table 2), and for the maximum and cut frequencies the values of 0.6 Hz and 0.4 Hz were selected, according to the indications in Prosek et al. (2002). The most important variables to which the procedure was applied are collected in Table 4, together with the computed AA values. The method was applied to both the TH-only and the NK/TH simulation results. For the former, being the core power a boundary condition, the first two values were not calculated since trivial. In Prosek et al. (2002), a second step of this methodology is reported. It allows to derive a condensed parameter (AA_{TOT}) globally determining the agreement of the simulation results and the experimental trends. It consists in a weighted average of the parameter accuracies (AA_p). However, the weights are based on engineering judgement and the ones proposed in the paper refer to Light Water Reactors. For this, the authors preferred to skip this second part of the procedure. Nevertheless, as visible from Table 4, all the parameter accuracies are well below the acceptability factor reported in Prosek et al. (2002), i.e., 0.4, thus, also their eventual weighted mean would be lower than it. In addition, the unweighted mean for the TH-only and NK/TH simulations are 0.045 and 0.063, respectively. The results in Table 4 demonstrate the good agreement between the simulation results and the experimental data for both cases.

4. Conclusions

This paper discussed the simulation results obtained by NERG of

Table 4
Parameter accuracies calculated with the FFTBM method, Prosek et al. (2002). In the following 'HL', 'CL' and 'BC' stand for 'Hot Leg', 'Cold Leg' and 'Boundary Condition'.

Variable	Description	AA (TH-Only)	AA (NK/TH)
V1	Fission Power	BC	0.095
V2	Decay Heat	BC	0.063
V3	PIOTA R2	0.040	0.074
V4	PIOTA R6	0.091	0.078
V5	L1 Prim. Mass Flow	0.036	0.022
V6	L1 Prim. HL Temp.	0.053	0.036
V7	L1 Prim. CL Temp.	0.026	0.044
V8	L1 Sec. CL Temp.	0.034	0.084
V9	L1 Sec. CL Temp.	0.038	0.071

Sapienza University of Rome during the open phase of the IAEA CRP on the FFTF LOFWOS Test #13. The novelty associated with the current simulation activity consists in the refinement of the TH model and, above all, the development of a 3D NK/TH coupled approach to study the transient behavior of liquid metal fast reactors. One of the main innovative aspects is related to the inclusion of the GEM NK/TH physical model, instead of a simple tabulation considering the component negative reactivity feedback as a function of the reactor mass flow. In addition, a detailed model of the assembly-to-bypass heat transfer has been prepared allowing a better simulation of the core radial temperature distribution.

With respect to the blind phase and the previous simulation activities, the RELAP5-3D© TH model was refined by considering two main aspects. The first is a detailed assembly-to-bypass heat transfer, differentiated for each row of core assemblies. It was obtained by refining the radial nodalization of the MULTID component representing the core bypass. In addition, the thermal inertia of the RTDs deputized to the data acquisition was accounted. In this case, dedicated heat structure components were added to the TH input deck. The first improvement allows a very good representation of the mid-term plateau characterizing the experimental trend of the row 6 PIOTA outlet temperature. Instead, the second implemented feature permits to precisely match the shape of all the loop temperature trends.

From the TH point of view, the only lasting open issues regard the secondary cold leg and the primary hot leg temperatures. In the first case, the code overpredicts the temperature of few degrees and an unidentified heat sink term seems to be present in the section going from the DHXs outlet to the point where the data is acquired (downstream the secondary pump). Referring to the primary hot leg temperature, the code predicts a mid/log-term increase while the experimental trend is nearly flat. This can be due to several phenomena, including the thermal stratification and the mixing convection within the RV outlet plenum, the thermal inertia of the submerged solid structures, and the heat losses. Unfortunately, the benchmark specifications do not provide the thermal–hydraulic data needed to fully characterize the sodium flow path going from the core outlet to the hot leg inlet, and this makes it difficult to identify the origin of the disagreement. To better match these two experimental trends, several sensitivity studies will be performed to identify the RV and HTS parameters that mostly affect their transient behavior.

In addition, the present paper described the complete NK model developed for the FFTF core by using the PHISICS code. The coupled codes results showed a good agreement with the experimental data. Some deviations were detected in the representation of the core power. Different potential error sources were identified, such as the constant K-coefficient introduced at the GEM assemblies inlet, the fuel and gap conductivities, etc. In the future development of the activity, several sensitivity studies are planned to evaluate the impact of these parameters on the simulation results and to determine the corresponding ranges that allow to refine the agreement with the benchmark data. In addition, it was highlighted the need to more precisely simulate some specific thermomechanical feedbacks that play a fundamental role in the accidental scenarios associated with the liquid metal fast reactors. In the prosecution of the activity, a nonlinear model of the thermomechanical deformations associated with the main elements of the core restraint system (i.e., diagrid, above core load pads, etc.) will be also added, as already done by other benchmark participants (Nikitin et al., 2024).

CRediT authorship contribution statement

Cristiano Ciurluini: Writing – review & editing, Writing – original draft, Methodology, Investigation, Formal analysis, Data curation, Conceptualization. **Michele Marra:** Writing – review & editing, Methodology, Investigation, Formal analysis, Data curation, Conceptualization. **Vincenzo Narcisi:** Writing – review & editing, Methodology, Investigation, Formal analysis, Data curation, Conceptualization.

Gianfranco Caruso: Writing – review & editing, Supervision, Methodology, Conceptualization. **Fabio Giannetti:** Writing – review & editing, Supervision, Methodology, Investigation, Formal analysis, Conceptualization.

Declaration of competing interest

The authors declare that they have no known competing financial interests or personal relationships that could have appeared to influence the work reported in this paper.

Data availability

The data that has been used is confidential.

Acknowledgements

References

Alfonsi, A., Epiney, A.S., Wang, Y., Balestra, P., Rabiti, C., 2019. PHISICS User Manual. INL-EXT-19-55002, Idaho Falls, Idaho, USA.

American Nuclear Society, 2005. American National Standard for decay heat power in light water reactors. ANSI/ANS-5.1-2005, La Grange Park, Illinois, USA.

Balestra, P., Parisi, C., Alfonsi, A., Rabiti, C., 2016. Simulation of AER-DYN-002 and AER-DYN-003 control rod ejection benchmarks by RELAP5-3D/PHISICS coupled codes. Nucl. Technol. 193 (1), 175–182. https://doi.org/10.13182/NT14-138.

Balestra, P., Alfonsi, A., Strydom, G., Rabiti, C., Giannetti, F., Caruso, G., 2017. Improvements to PHISICS/RELAP5-3D© capabilities for simulating HTGRs. Trans. Am. Nucl. Soc. 116, 1009–1012.

Chen, X.-N., Rineiski, A., 2023. SIMMER modelling of accident initiation phase in sodium fast reactors. Nucl. Eng. Des. 409, 112351 https://doi.org/10.1016/j.nucengdes.2023.112351.

Cheng, S.K., Todreas, N.E., 1986. Hydrodynamic models and correlations for bare and wire-wrapped hexagonal rod bundles - Bundle friction factors, subchannel friction factors and mixing parameters. Nucl. Eng. Des. 92, 227–251. https://doi.org/10.1016/0029-5493(86)90249-9.

Ciurluini, C., Narcisi, V., Giannetti, F., Cretara, L., Caruso, G., 2020. Preliminary neutron kinetic – thermal hydraulic coupled analysis of the ALFRED reactor using PHISICS/RELAP5-3D. J. Phys. Conf. Ser. 1599, 012023 https://doi.org/10.1088/1742-6596/1599/1/012023.

Del Nevo, A., Martelli, E., 2016. Validation of a three-dimensional model of EBR-II and assessment of RELAP5-3D based on SHRT-17 Test. Nucl. Technol. 193, 1–14. https://doi.org/10.13182/NT14-152.

Gerschenfeld, A., Gorsse, Y., Li, S., 2023. Multiscale Effects in Sodium Fast Reactors : Feedback from the Open Phase of the FFTF LOFWOS-13 Test. Proc. of the 20th International Topical Meeting on Nuclear Reactor Thermal Hydraulics (NURETH-20), August 20–25, 2023. Washington, D.C., USA, https://doi.org/10.13182/NURETH20-40892.

Hamase, E., Ohgama, K., Kawamura, T., Doda, N., Tanaka, M., Yamano, H., 2024. Validation of the fast reactor plant dynamics analysis code Super-COPD using FFTF loss of flow without scram test #13. Ann. Nucl. Energy 195, 110157. https://doi.org/10.1016/j.anucene.2023.110157.

Hong, J., Tak, N.-I., Hong, S.L., Eoh, J., 2024. Validation of GAMMA+ code for SFR application using FFTF loss-of-flow-without-scram test results. Nucl. Eng. Des. 417, 112816 https://doi.org/10.1016/j.nucengdes.2023.112816.

IAEA, International Atomic Energy Agency, 2018. Benchmark Analysis of FFTF Loss of Flow Without Scram Test. https://www.iaea.org/projects/crp/i32011.

Idelchik, I.E., 1986. Handbook of Hydraulic Resistance, second ed. Hemisphere Publishing Corporation.

Kazimi, M.S., Carelli, M.D., 1976. Clinch River Breeder Reactor Plant Heat Transfer Correlation for Analysis of CRBRP Assemblies. CRBRP-ARD-0034, Westinghouse.

Liu, Y., Mui, T., Xie, Z., Hu, R., 2023. Benchmarking FFTF LOFWOS Test# 13 using SAM code: Baseline model development and uncertainty quantification. Ann. Nucl. Energy 192, 110010. https://doi.org/10.1016/j.anucene.2023.110010.

Lucoff, D.M., 1989. Passive safety testing at the fast flux test facility. Nucl. Technol. 88 (1), 21–29. https://doi.org/10.13182/NT89-A34333.

Lyu, S., Lu, D., Sui, D., 2021. Benchmark analysis on loss-of-flow-without-scram test of FFTF using refined SAC-3D models. Sci. Technol. Nucl. Install. 2021, 5843910. https://doi.org/10.1155/2021/5843910.

Mascari, F., Vella, G., Woods, B.G., Welter, K., Pottorf, J., Young, E., Adorni, M., D'Auria, F., 2011. Sensitivity analysis of the MASLWR helical coil steam generator using TRACE. Nucl. Eng. Des. 241 (4), 1137–1144. https://doi.org/10.1016/j.nucengdes.2010.05.002.

Moisseytsev, A., Sumner, T., 2022. Impact of assembly-to-assembly heat transfer on the simulation results of FFTF LOFWOS test. Proc. International Topical Meeting on Nuclear Reactor Thermal Hydraulics 19 (NURETH-19), March 6–11, Brussels, Belgium.

Morelová, N., Kriventsev, V., Sumner, T., Moisseytsev, A., Heidet, F., Wootan, D.W., Casella, A.M., Nelson, J.V., Di Piazza, I., Hassan, H., Lorusso, P., Martelli, D., Yang, X., Wang, J., Lu, D., Zhang, D., Gerschenfeld, A., Kliem, S., Fridman, E., Rineiski, A., Kumaresan, N., Giannetti, F., Petruzzi, A., Tanaka, M., Jeong, J.-H., Hong, J., Stempniewicz, M., Tsaun, S., Volkov, A., Wallenius, J., Fiorina, C., Mikityuk, K., Vaghetto, R., Omotowa, O., Kelly, J., Lane, J., 2023. IAEA'S coordinated research projects on thermal hydraulics of fast reactors. Proc. International Conference on Nuclear Engineering (ICONE), May 21-26, Kyoto, Japan, 10.1299/jsmeicone.2023.30.1632.

Narcisi, V., Giannetti, F., Caruso, G., 2019. Investigation on RELAP5-3D© capability to predict thermal stratification in liquid metal pool-type system and comparison with experimental data. Nucl. Eng. Des. 352, 110152 https://doi.org/10.1016/j.nucengdes.2019.110152.

Narcisi, V., Giannetti, G., Subioli, A., Del Nevo, A., Caruso, G., 2020a. Assessment of a RELAP5-3D three-dimensional analysis based on PHÉNIX dissymmetric transient test. J. Nuc. Eng. Rad. Sci. 6, 011301 https://doi.org/10.1115/1.4044847.

Narcisi, V., Giannetti, F., Caramello, M., Caruso, G., 2020b. Preliminary evaluation of ALFRED revised concept under station blackout. Nucl. Eng. Des. 364, 110648 https://doi.org/10.1016/j.nucengdes.2020.110648.

Narcisi, V., Ciurluini, C., Giannetti, F., Caruso, G., 2021. Thermal-hydraulic transient analysis of the FFTF LOFWOS Test #13. Nucl. Eng. Des. 383, 111405 https://doi.org/10.1016/j.nucengdes.2021.111405.

Nguyen, D.H., 1990. Role of feedback reactivities in the passive safety of nuclear reactors: the case of the Fast Flux Test Facility. Nucl. Technol. 91, 61–74. https://doi.org/10.13182/NT90-A34441.

Nikitin, E., Fridman, E., Ponomarev, A., 2024. Analysis of loss of flow without scram test in the FFTF reactor – Part I: Preparation of neutronics data. Prog. Nucl. Energy 168, 105018. https://doi.org/10.1016/j.pnucene.2023.105018.

OECD Nuclear Energy Agency, 2014 Technology Roadmap Update for Generation IV Nuclear Energy Systems 1-66. Available online at: https://www.gen-4.org/gif/upload/docs/application/pdf/2014-03/gif-tru2014.pdf. Last visited 11/01/2024.

Prosek, A., D'Auria, F., Mavko, B., 2002. Review of quantitative accuracy assessments with fast Fourier transform based method (FFTBM). Nucl. Eng. Des. 217, 179–206. https://doi.org/10.1016/S0029-5493(02)00152-8.

Radman, S., Fiorina, C., Song, P., Pautz, A., 2022. Development of a point-kinetics model in OpenFOAM, integration in GeN-Foam, and validation against FFTF experimental data. Ann. Nucl. Energy 168, 108891. https://doi.org/10.1016/j.anucene.2021.108891.

Rimpault, G., Plisson, D., Tommasi, J., Jacqmin, R., Rieunier, J.-M., Verrier, D., Biron, D., 2002. The ERANOS Code and data system for fast reactor neutronic analyses. Proc. International Conference on the New Frontiers of Nuclear Technology: Reactor Physics, Safety and High-Performance Computing (PHYSOR 2002), October, Seoul, South Korea.

Rivas, A., Stauff, N., Sumner, T., Hou, J., 2021. Propagating neutronic uncertainties for FFTF LOFWOS Test #13. Nucl. Eng. Des. 375, 111047 https://doi.org/10.1016/j.nucengdes.2020.111047.

Seban, R.A., Shimazaki, T.T., 1951. Heat transfer to a fluid flowing turbulently in a smooth pipe with walls at constant temperature. T. ASME 73, 803–809.

Sha, W.T., Launder, B.E., 1979. A model for turbulent momentum and heat transport in large rod bundles. ANL-77-73. Argonne National Laboratory, IL, USA.

Sumner, T., 2018. Benchmark analysis of fast flux test facility (FFTF) loss of flow without scram test. ANL-ART-102-Rev.2, IAEA CRP- I31032, ANL, USA.

Tenchine, D., Pialla, D., Fanning, T.H., Thomas, J.W., Chellapandi, P., Shvetsov, Y., Maas, L., Jeong, H.-Y., Mikityuk, K., Chenu, A., Mochizuki, H., Monti, S., 2013. International benchmark on the natural convection test in Phenix reactor. Nucl. Eng. Des. 258, 189–198. https://doi.org/10.1016/j.nucengdes.2013.02.010.

The RELAP5-3D© Code Development Team, 2015a. RELAP5-3D Code Manual Vol. I: Code Structure, System Models, and Solution Methods. INL/MIS-15-36723 Volume I, Revision 4.3, Idaho Falls, Idaho, USA.

The RELAP5-3D© Code Development Team, 2015b. RELAP5-3D Code Manual Vol. IV: Models and Correlations. INL/MIS-15-36723 Volume IV, Revision 4.3, Idaho Falls, Idaho, USA.

Vikram, G., Riyas, A., Bachchan, A., Rajendrakumar, M., Devan, K., Natesan, K., 2023. Modeling of sodium-cooled fast reactor core – A sensitivity study on number of core channels and axial meshes. Nucl. Eng. Des. 403, 112136 https://doi.org/10.1016/j.nucengdes.2022.112136.

Wang, S., Mikityuk, K., Dorde, P., Zhang, D., Su, G., Qiu, S., Tian, W., 2021. Validation of TRACE capability to simulate unprotected transients in Sodium Fast Reactor using FFTF LOFWST Test #13. Ann. Nucl. Energy 164, 108600. https://doi.org/10.1016/j.anucene.2021.108600.

Wootan, D.W., Omberg, R.P., Sofu, T., Grandy, C., 2017a. Passive safety testing at the fast flux test facility relevant to new LMR designs. Proc. International Conference on Fast Reactor and Related Fuel Cycles, June 26-29, Yekaterinburg, Russia.

Wootan, D.W., Omberg, R.P., Grandy, C., 2017b. The U.S. knowledge preservation program for fast flux test facility data. Proc. International Conference on Fast Reactor and Related Fuel Cycles, June 26-29, Yekaterinburg, Russia.

Zhou, L., Zhang, D., Wang, S., Liu, Y., Liang, Y., Zhang, J., Tian, W., Qiu, S., Su, G., 2023. Benchmark analysis of the FFTF LOSWOS test #13 with OpenMC and THACS. Ann. Nucl. Energy 194, 110087. https://doi.org/10.1016/j.anucene.2023.110087.

Zigrang, D.J., Sylvester, N.D., 1985. A review of explicit friction factor equations. J. Energ. Resour.-ASME 107, 280–283.